X-RAY SPECTRAL VARIATION OF η CARINAE THROUGH THE 2003 X-RAY MINIMUM

Kenji Hamaguchi,[1,2] Michael F. Corcoran,[1,2] Theodore Gull,[3] Kazunori Ishibashi,[4]
Julian M. Pittard,[5] D. John Hillier,[6] Augusto Damineli,[7] Kris Davidson,[8]
Krister E. Nielsen,[3,9] and Gladys Vieira Kober[3,9]

ABSTRACT

We report the results of an observing campaign on η Car around the 2003 X-ray minimum, mainly using the *XMM-Newton* observatory. These are the first spatially resolved X-ray monitoring observations of the stellar X-ray spectrum during the minimum. The hard X-ray emission, associated with the wind-wind collision (WWC) in the binary system, varied strongly in flux on timescales of days, but not significantly on timescales of hours. The X-ray flux in the 2–10 keV band seen by *XMM-Newton* was only 0.7% of the flux maximum seen by *RXTE*. The slope of the X-ray continuum above 5 keV did not vary in any observation, which suggests that the electron temperature of the hottest plasma did not vary significantly at any phase. Through the minimum, the absorption to the stellar source increased by a factor of 5–10 to $N_{\rm H} \sim (3-4) \times 10^{23}$ cm^{-2}. These variations were qualitatively consistent with emission from the WWC plasma entering into the dense wind of the massive primary star. During the minimum, X-ray spectra also showed significant excesses in the thermal Fe xxv emission line on the red side, while they showed only a factor of 2 increase in equivalent width of the Fe fluorescence line at 6.4 keV. These features are not fully consistent with the eclipse of the X-ray plasma and may suggest an intrinsic fading of the X-ray emissivity. The drop in the WWC emission revealed the presence of an additional X-ray component that exhibited no variation on timescales of weeks to years. This component may be produced by the collision of high-speed outflows at $v \sim 1000-2000$ km s^{-1} from η Car with ambient gas within a few thousand AU from the star.

Subject headings: binaries: general — stars: early-type — stars: individual (η Carinae) — stars: winds, outflows — X-rays: stars

1. INTRODUCTION

η Carinae is a violently unstable, extremely luminous object and a key tracer of evolution of stars in the upper portion of the Hertzsprung-Russell diagram (Davidson & Humphreys 1997). The star is believed to have had an initial mass of $\gtrsim 150$ $M_\odot$ (Hillier et al. 2001). It is currently in a short, poorly understood evolutionary stage, known as the luminous blue variable (LBV) phase, which is thought to occur near the onset of pulsational instabilities. It provides a convenient laboratory to study how extremely luminous, massive stars evolve and how they shape their environments both geometrically and chemically.

η Car is best known for an extraordinarily powerful eruption in 1843 that sent ~ 12 $M_\odot$ (Smith et al. 2003b) of its atmosphere into space, creating a beautiful bipolar nebulosity called the Homunculus around the star. η Car also had a minor eruption in 1890, which produced a small bipolar nebula inside the Homunculus Nebula (the ''Little Homunculus;'' Ishibashi et al. 2003). The star still exhibits a strong mass loss (10^{-4} to

10^{-3} $M_\odot$ yr^{-1}; Davidson et al. 1995; Cox et al. 1995; Ishibashi et al. 1999; Hillier et al. 2001; Pittard & Corcoran 2002), preferentially in the polar direction (Smith et al. 2003a; van Boekel et al. 2003). The ejecta and the stellar wind are rich in helium and nitrogen and depleted in oxygen and carbon (Verner et al. 2005; Davidson et al. 1984; Hillier et al. 2001), consistent with CNO processing. Davidson et al. (2005) and Martin & Koppelman (2004) suggested from the change of Hα and Hβ line profiles and the increase of optical brightness that η Car is changing rapidly at the present time.

The past decade has witnessed an important change in our understanding of the star. This began with the recognition that the strength of some narrow emission lines, notably He i λ10830, vary predictably with a period of 5.52 yr (Damineli 1996). Along with observations in infrared (Whitelock et al. 1994; Feast et al. 2001), millimeter (Cox et al. 1995), centimeter (Duncan et al. 1995), and optical (van Genderen et al. 1999) wavelengths, observations of the X-ray emission from the star have played a key role. *Röntgensatellit* (*ROSAT*) observations in 1992 first showed a variation that appeared to be correlated with Damineli's emission-line variations (Corcoran et al. 1995), and subsequently the 2–10 keV light curve of the star obtained by the *Rossi X-Ray Timing Explorer* (*RXTE*; Ishibashi et al. 1999) showed in detail the X-ray variation culminating in a swift, unstable rise to maximum and steep fall to minimum lasting for ~ 3 months, i.e., the same time interval as Damineli's spectroscopic minimum. These observations clearly show that the star varies in a fundamental way every 5.54 yr, and they strongly suggest that η Car is two stars, not one. In this binary model, most of the dramatic, panchromatic changes are now believed to be produced by the interaction of the UV flux and wind from a companion star with the wind of η Car. Variations in the X-ray region are produced by a wind-wind collision (WWC)

[1] CRESST and X-Ray Astrophysics Laboratory, NASA Goddard Space Flight Center, Greenbelt, MD 20771; kenji@milkyway.gsfc.nasa.gov.
[2] Universities Space Research Association, Columbia, MD 21044.
[3] Astrophysics Science Division, NASA Goddard Space Flight Center, Greenbelt, MD 20771.
[4] Kavli Institute for Astrophysics and Space Research, Massachusetts Institute of Technology, Cambridge, MA 02139.
[5] School of Physics and Astronomy, University of Leeds, Leeds LS2 9JT, UK.
[6] Department of Physics and Astronomy, University of Pittsburgh, Pittsburgh, PA 15260.
[7] Departamento de Astronomia do IAGUSP, 05508-900 São Paulo, Brazil.
[8] Astronomy Department, University of Minnesota, Minneapolis, MN 55455.
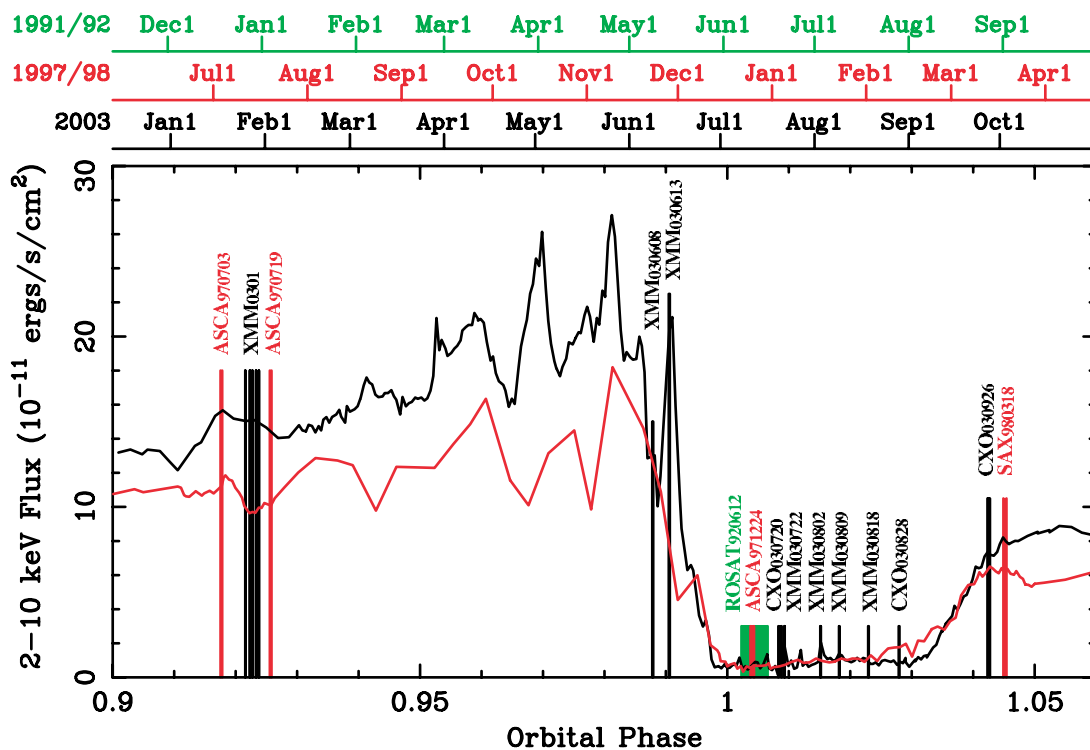[9] Catholic University of America, Washington, DC 20064.

Fig. 1.—*RXTE* light curves (*black solid lines*: 2003; *red solid lines*: 1997/1998) around the X-ray minimum with the timings of *XMM-Newton*, *Chandra*, *ASCA*, *BeppoSAX*, and *ROSAT* pointed observations (*black*: 2003; *red*: 1997/1998; *green*: 1992). Multiple *ROSAT* observations between 1.00 and 1.01 were summed together for ROSAT$_{920612}$.

of the wind from η Car with the wind of the companion star. A current guess at the system parameters describes a massive hot companion with $M_c \sim 30\ M_\odot$ plus a brighter primary star with $M_\eta \geq 80\ M_\odot$ in a highly eccentric ($e > 0.9$), 5.54 yr orbit (Corcoran et al. 2001a; see also Davidson 1999).

During the 1997/1998 X-ray minimum, η Car was the target of every available X-ray observatory, including *RXTE* (Ishibashi et al. 1999; Corcoran et al. 2001a), *ASCA* (Corcoran et al. 2000), and *BeppoSAX* (Viotti et al. 2002). The *ASCA* satellite detected hard X-ray emission from η Car (Corcoran et al. 2000), which was characterized by slightly smaller N_H than the pre-minimum state with reduced plasma emission measure (EM). The limited spatial resolution of *ASCA*, however, left the possibility that the observed emission was due to contamination by unresolved nearby sources. The *BeppoSAX* satellite observed η Car just after the recovery of the X-ray emission (Viotti et al. 2002). The spectrum showed strong absorption of $N_H \sim 1.5 \times 10^{23}$ cm^{-2}, unlike the *ASCA* spectrum during the minimum, which had an $N_H \sim 3 \times 10^{22}$ cm^{-2}. The overall X-ray brightness variations observed with *RXTE* are explained well with the colliding wind mechanism (Pittard et al. 1998; Pittard & Corcoran 2002). However, key properties of the X-ray light curve were still poorly understood: dramatic changes in X-ray flux as the emission increases to maximum, the variation of the absorbing material in front of the X-ray-emitting region near the X-ray minimum, the nature of the rapid fall from X-ray maximum to X-ray minimum, and the excess in N_H after recovery.

The minimum that occurred in mid-2003 was among the best-observed astronomical events of all time. A key part of this campaign were the detailed X-ray observations obtained with *RXTE*, *Chandra*, and *XMM-Newton*. *RXTE* again provided crucial monitoring of the daily changes in X-ray flux, while *Chandra* provided previously unobtainable monitoring of the X-ray emission

line dynamics at key phases of the binary period. *XMM-Newton* obtained critical measurements of the spectrum of the source during the low-flux state when observations with *RXTE* or *Chandra* are difficult.

This paper describes the overall change of the X-ray spectrum of η Car around the 2003 minimum as measured by *XMM-Newton* (Jansen et al. 2001), supplemented where necessary with key observations with *Chandra* (Weisskopf et al. 2002). We try to understand the X-ray emission and absorption mechanism and the cause of the X-ray minimum, from a comparison of derived spectral properties such as kT, N_H, and emission-line strengths in these observations and earlier *ROSAT* and *ASCA* observations during the 1992 and 1997/1998 minima.

The paper is comprised of the following sections. Section 2 describes the observations and method of the data reduction and includes a description of problems of unresolved emission components around the central source in the extracted *XMM-Newton* source events. Section 3 describes imaging and timing analyses of the *XMM-Newton* data. Section 4 describes the analysis of the X-ray spectra during the 2003 minimum. Section 5 compares the X-ray spectra during the 2003 minimum to the previous minima in 1998 and 1992. We discuss our results in § 6, and in § 7 we summarize our conclusions.

2. OBSERVATIONS AND DATA REDUCTION

In 2003, *XMM-Newton* observed η Car a total of 11 times, five times in 2003 January (about 6 months before the onset of the 2003 minimum), twice in 2003 June (weeks before the onset of the 2003 minimum, near the X-ray maximum), and four times during the 2003 minimum in 2003 July and August prior to the recovery, which started near 2003 September 3. Figure 1 displays these observing times on the *RXTE* light curve (Corcoran 2005) for context. We also reanalyzed two *XMM-Newton* observations from

TABLE 1
Logs of the *XMM-Newton* and *Chandra* Observations

Abbreviation (1)	Sequence ID (2)	Observation Start		Exposure (ks) (5)	Observation Mode (6)	Filter (7)
		Date (3)	ϕ_{orbit} (4)			
Before the Minimum						
XMM$_{000726}$[a]	112580601	2000 Jul 26, 06:01 (M2)	0.470	.../.../29.6	PFW/PFW/PSW	Thick
XMM$_{000728}$[a]	112580701	2000 Jul 28, 00:51 (M2)	0.471	.../.../7.8	PFW/PFW/PSW	Thick
XMM$_{030125}$[b]	145740101	2003 Jan 25, 13:03 (pn)	0.922	4.8/.../...	PSW/PFW/PFW	Thick
XMM$_{030127A}$[b]	145740201	2003 Jan 27, 01:08 (pn)	0.922	4.8/.../...	PSW/PFW/PFW	Thick
XMM$_{030127B}$[b]	145740301	2003 Jan 27, 20:42 (pn)	0.923	4.7/.../...	PSW/PFW/PFW	Thick
XMM$_{030129}$[b]	145740401	2003 Jan 29, 01:45 (pn)	0.923	5.8/.../...	PSW/PFW/PFW	Thick
XMM$_{030130}$[b]	145740501	2003 Jan 30, 00:00 (pn)	0.924	4.8/.../...	PSW/PFW/PFW	Thick
XMM$_{030608}$	160160101	2003 Jun 08, 13:31 (M1)	0.988	22.1/27.6/...	PSW/PSW/PFW	Thick
XMM$_{030613}$	160160901	2003 Jun 13, 23:52 (M1)	0.990	21.9/30.4/...	PSW/PSW/PFW	Thick
During the Minimum						
CXO$_{030720}$[c]	200216	2003 Jul 20, 01:47	1.008	90.3	ACIS-S w/HETG	...
XMM$_{030722}$[c]	145780101	2003 Jul 22, 01:51 (M2)	1.009	5.8/8.2/8.4	PSW/PSW/PFW	Thick
XMM$_{030802}$	160560101	2003 Aug 02, 21:01 (M2)	1.015	12.2/17.1/17.5	PSW/PSW/PFW	Thick
XMM$_{030809}$	160560201	2003 Aug 09, 01:44 (M2)	1.018	8.7/12.3/12.6	PSW/PSW/PFW	Thick
XMM$_{030818}$	160560301	2003 Aug 18, 15:23 (M2)	1.023	13.0/18.2/18.6	PSW/PSW/PFW	Thick
CXO$_{030828}$	200237	2003 Aug 28, 17:38	1.028	18.8	ACIS-S	...
After the Minimum						
CXO$_{030926}$	200217	2003 Sep 26, 22:47	1.042	70.1	ACIS-S w/HETG	...

Notes.—Col. (1): Abbreviation adopted for each observation. Col. (2): Sequence identification number of each observation. Col. (3): Start time of the detector in the parentheses. Col. (4): $\phi_{orbit} = (JD[\text{observation start}] - 2,450,799.792)/2024$ (Corcoran 2005). Col. (5): Exposure time excluding the detector dead time; for *XMM-Newton* observations the exposure times are given for the pn, MOS1, and MOS2 detectors, respectively; the data sets without exposure time were not used due to the severe event pileup. Col. (6): Observation mode; PSW: prime small window; PFW: prime full window. For the *XMM-Newton* observations the observation modes are given for the pn, MOS1, and MOS2 detectors, respectively. Col. (7): Optical blocking filter selected for the *XMM-Newton* detectors.
[a] Data from XMM$_{000726}$ and XMM$_{000728}$ are combined and denoted as XMM$_{0007}$.
[b] Data from XMM$_{030125}$, XMM$_{030127A}$, XMM$_{030127B}$, XMM$_{030129}$, and XMM$_{030130}$ are combined and denoted as XMM$_{0301}$.
[c] Spectra from CXO$_{030720}$ and XMM$_{030722}$ are simultaneously fitted and those results are denoted as CXOXMM$_{0307}$.

2000, whose results were previously published by Leutenegger et al. (2003). We thus used a total of 13 *XMM-Newton* observations in our analysis, as listed in Table 1. Throughout this paper, individual *XMM-Newton* observations are designated XMM, subscripted with the year, month, and day of the observation. To improve statistics, we combined data from two observations in 2000 and combined data from five observations in 2003 January because these observations were close together in time and did not show any significant variability among them.

XMM-Newton is composed of three nested Wolter I–type X-ray telescopes (Aschenbach et al. 2000) with the European Photon Imaging Camera (EPIC) CCD detectors (pn, MOS1, and MOS2) in their focal planes (Strüder et al. 2001; Turner et al. 2001). In all the observations, η Car was on-axis but the observations were obtained with different satellite roll angles. The EPIC instrumental modes are listed in Table 1. The *XMM-Newton* spectra suffered significant photon pileup in the data taken in prime full window (PFW) mode outside the 2003 minimum when the star was bright in the 2–10 keV band. We did not use these data sets in our analysis. *XMM-Newton* is also equipped with the Reflection Grating Spectrometer (RGS; den Herder et al. 2001), but the RGS has limited sensitivity above $\sim$1 keV, where emission from the WWC region dominates. We therefore did not use the RGS data.

The analysis of the *XMM-Newton* data was performed with version 5.4.1 of the SAS[10] software package and version 5.2 of

the HEASoft[11] analysis package. The Observation Data Files (ODF) data were processed using the SAS scripts "emchain" and "epchain." We removed events close to hot pixels or outside the field of view and selected events with pattern $\leqq$4 for EPIC pn spectral analysis and pattern $\leqq$12 for timing analysis of the EPIC pn data and spectral and timing analysis of the EPIC MOS data. Most of these observations luckily avoided high background periods, and the instrumental background is negligible in any observations within the 0.3–10 keV band. We did not need to reject any high background periods because the strong emission from η Car greatly surpassed the observed background levels.

Due to the limited spatial resolution of *XMM-Newton*, the extracted η Car data inevitably include emission from a number of sources (see Fig. 2). The extracted spectrum is usually dominated by hard X-rays from the WWC in η Car, which varies from observation to observation (Corcoran et al. 2000; Viotti et al. 2002). The Homunculus Nebula emits weak diffuse reflected X-rays from the central source, which can be spatially resolved only with *Chandra* and only during the minimum (Corcoran et al. 2004). The outer ejecta extending about 1′ beyond the Homunculus Nebula emits diffuse nonvariable X-rays below $\sim$1 keV with a ring- or shell-like morphology (Seward et al. 2001; Weis et al. 2004). To correct the *XMM-Newton* spectra for emission from the outer ejecta and the Homunculus Nebula, we used three *Chandra* data sets from the 2003 X-ray observing campaign, two observations

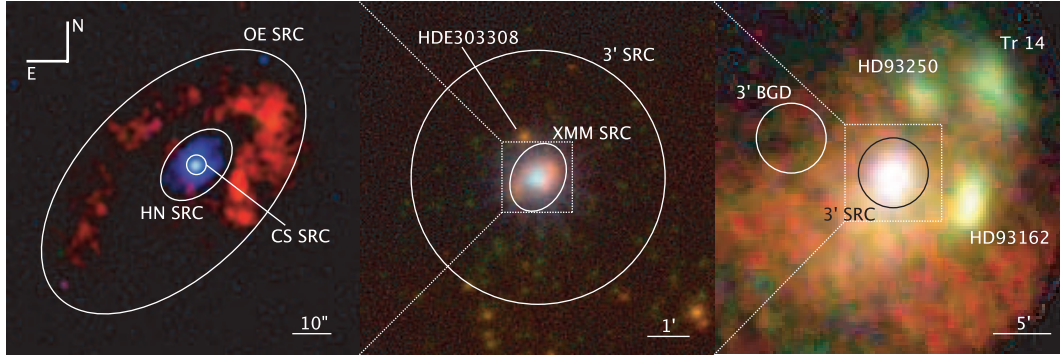[10] See http://xmm.vilspa.esa.es/external/xmm_sw_cal/sas_frame.shtml.

[11] See http://heasarc.gsfc.nasa.gov/docs/software/lheasoft/.

Fig. 2.—True color images of η Car. *Left*: *Chandra* HETG zeroth-order data from CXO$_{030720}$ (*red*: 0.2–1 keV; *green*: 1–3 keV; *blue*: 3–10 keV). *Middle*: *XMM-Newton* image accumulated from all the available MOS data taken in PFW mode (*red*: 0.2–1 keV; *green*: 1–3 keV; *blue*: 3–9 keV). *Right*: *ASCA* GIS data from ASCA$_{971224}$ (*red*: 0.8–1 keV; *green*: 1–3 keV; *blue*: 3–10 keV). The color in the *ASCA* image has been chosen to highlight the diffuse emission. Solid lines show source (SRC) or background (BGD) regions (designations: OE=outer ejecta, HN=Homunculus Nebula, CS=central source). The *Chandra* and *ASCA* images were smoothed with a Gaussian with $\sigma = 1.5$ pixels, while the *XMM-Newton* image was not smoothed.

during the 2003 minimum and an observation just after the 2003 minimum. These *Chandra* observations spatially resolve the outer ejecta emission from the emission of the stellar source and so allow us to determine the spectrum of the outer emission, which we can then use to help model the *XMM-Newton* spectra.

The log of *Chandra* observations and the timing of the observations are also given in Table 1 and Figure 1. *Chandra* observations are designated CXO, subscripted with the year, month, and day of the observation, similar to our designation of the *XMM-Newton* observations. The *Chandra* observations were obtained using the Advanced CCD Imaging Spectrometer detector using the Spectrometer array (ACIS-S) either with or without the High Energy Transmission Grating (HETG). For the grating data, zeroth-order photon events were used for CXO$_{030720}$ (during the X-ray minimum, when the source was too faint at first order), and first-order photon events were used for CXO$_{030926}$ after the recovery since the central source had severe pileup in the zeroth-order data. The observation CXO$_{030828}$, taken during the minimum with the ACIS-S imaging array with no grating, also suffered mild pileup (∼4%). The analysis of the *Chandra* data was performed with the CIAO[12] software package, version 2.3 (CALDB ver. 2.22), version 3.0 (CALDB ver. 2.23), and version 3.0.2 (CALDB ver. 2.26) for sequences 200216, 200237, and

200217, respectively. We also used version 5.2 of the HEAsoft package and followed the recommendations of the analysis science thread.[13] A full analysis of the *Chandra* spectra will be published separately (M. F. Corcoran et al. 2007, in preparation).

3. X-RAY IMAGES AND TIME VARIABILITY

All *XMM-Newton* images similarly showed emission from the central source and the outer ejecta (Fig. 2). Because these *XMM-Newton* images cannot completely separate emission from the outer ejecta and central source nor resolve the faint X-ray Homunculus Nebula (Corcoran et al. 2004), we used an ellipse of $50'' \times 37.5''$ as the source region (called ''XMM SRC'' in Fig. 2), which includes all these emission components but excludes nearby X-ray–luminous stars (such as HDE 303308) more than ∼1′ distant. For some small window mode MOS observations, the southeast tip of the ellipse fell outside the small window. We determined background using regions from apparently source-free regions on the same CCD chip.

Table 2 shows detected photon count rates in the soft (0.3–1 keV), medium (1–4 keV), and hard (4–10 keV) bands in each detector for each observation. The soft band mainly includes emission from the outer ejecta, while the medium band includes emission from an additional source that we call the central constant emission component (CCE; see § 4.1.2), and the medium

---

[12] See http://cxc.harvard.edu/ciao/.

[13] See http://cxc.harvard.edu/ciao/threads.

TABLE 2
Time Variability

| | NET COUNT RATE (counts s^{-1}) | | | | | | | | | CONSTANT MODEL FIT χ^2/dof | | | |
| | SOFT (0.3–1 keV) | | | MEDIUM (1–4 keV) | | | HARD (4–10 keV) | | | | | | |
OBSERVATION	pn	MOS1	MOS2	pn	MOS1	MOS2	pn	MOS1	MOS2	Soft	Medium	Hard	dof
XMM$_{0007}$	...	...	0.255[a]	...	...	1.25[a]	...	...	0.91[a]	0.97	1.12	0.82	76
XMM$_{0301}$	1.15	...	...	7.72	...	...	7.18	...	...	0.98	1.14	1.05	75
XMM$_{030608}$	1.10	0.247[a]	...	4.58	1.70[a]	...	6.77	1.89[a]	...	0.99	1.45	0.95	55
XMM$_{030613}$	1.09	0.242[a]	...	4.99	1.84[a]	...	10.49	2.80[a]	...	1.02	1.84	1.29	62
XMM$_{030722}$	1.03	0.223[a]	0.285	0.456	0.170[a]	0.188	0.183	0.045[a]	0.049	0.81	0.85	1.31	16
XMM$_{030802}$	1.07	0.222[a]	0.288	0.464	0.161[a]	0.190	0.517	0.137[a]	0.124	0.97	1.21	0.75	34
XMM$_{030809}$	1.06	0.226[a]	0.280	0.476	0.178[a]	0.188	0.554	0.159[a]	0.151	1.13	0.79	1.09	24
XMM$_{030818}$	1.05	0.221[a]	0.288	0.514	0.169[a]	0.202	0.648	0.179[a]	0.174	1.34	0.96	0.92	37

[a] Source regions are slightly smaller for these Prime Small Window observations.
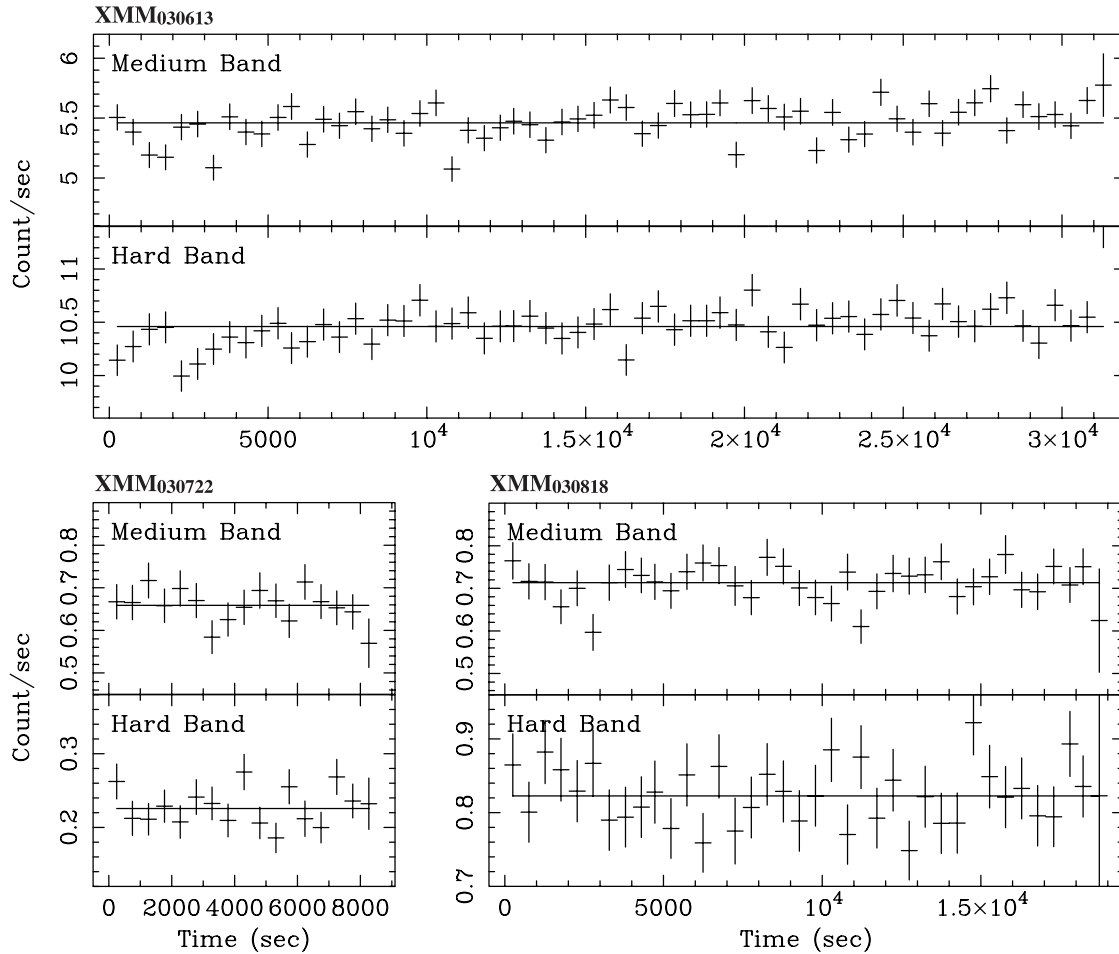
FIG. 3.—Background-subtracted EPIC pn+MOS light curves from XMM_{030613} (*top*), XMM_{030722} (*bottom left*), and XMM_{030818} (*bottom right*). Top and bottom graphs in each panel show the medium (1–4 keV) and hard (4–10 keV) bands, respectively. A solid line in each panel shows the best-fit constant model.

band outside the minimum and the hard band includes the WWC emission (see § 4.2). In the soft band, the MOS2 count rates are 10% lower in XMM_{0007} than during the 2003 minimum because of the use of a smaller MOS2 source region for the XMM_{0007} data. The soft-band pn count rates are slightly higher outside minimum because the spectral response of the pn allows photons from the bright hard source to contaminate the soft band. For example, we estimate the soft-band contamination due to the hard photons in XMM_{0007} to be ~0.08 counts s^{-1}, which makes the corrected pn count rates in the soft band 1.06 counts s^{-1} in this observation. This means that the emission from the outer ejecta was constant to ≲2% to better than 90% confidence over a half-year interval. On the other hand, both the medium- and hard-band count rates decreased dramatically to ~1%–5% of the maximum brightness seen by *XMM-Newton*.

We constructed light curves with 500 s time bins, combining all the available MOS and pn data. In Figure 3 we show three sample light curves, representing variations before the minimum (XMM_{030613}) and during the minimum (XMM_{030722}, XMM_{030818}). In general, these light curves showed no significant variation in most energy bands at >90% confidence (Table 2, Fig. 3). The exceptions are the medium-band light curves before the 2003 minimum. The medium-band light curve from the XMM_{030608} observation showed an "excess" of ~0.2 counts s^{-1} (~4%) near the middle of the observation, while the medium-band light curve from the XMM_{030613} observation showed a slight linear increase by ~$0.54^{+0.21}_{-0.22}$ counts s^{-1} day^{-1} (1 σ), or ~10% day^{-1}. The

linear model is still not accepted above the 90% confidence level (χ^2/dof = 1.59), due to small fluctuation on timescales of ≲500 s. We note that the hard-band light curve in XMM_{030613} is also better reproduced by a linearly increasing model with a slope of ~$0.78^{+0.32}_{-0.26}$ counts s^{-1} day^{-1}, or ~7.5% day^{-1}, with χ^2/dof = 0.98. This increase is roughly consistent with the *RXTE* light curve (~15% day^{-1}; see Fig. 1).

4. X-RAY SPECTRA

For each *XMM-Newton* observation, we produced EPIC pn and MOS spectra using the same source and background regions as in § 3. Figure 4 presents the EPIC pn spectra for all 2003 observations. The X-ray spectra are a combination of a variable hard WWC component along with nonvariable emission from a number of components. Consistent with Table 2, the spectra below 1 keV are almost constant through the observations. Above 1 keV the spectra varied by a factor of 2–3 before the 2003 minimum, then decreased dramatically by more than an order of magnitude after the onset of the 2003 minimum in June, with small recovery by a factor of ~3 at $E \gtrsim 4$ keV during August. Most spectra clearly showed lines of hydrogen- and helium-like ions of Mg, Si, S, Ar, Ca, Fe, and Ni and a fluorescence line from cold Fe.

In the following we first examine the nonvariable emission and then use this emission to fully understand changes in the variable component. In our analysis, we adopt abundances relative to solar abundances given by Anders & Grevesse (1989).
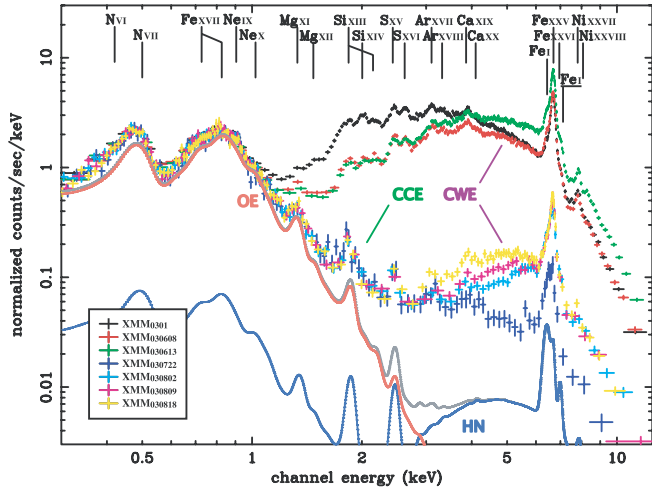
Fig. 4.—*XMM-Newton* EPIC pn spectra of η Car in 2003. The central source (central constant emission [CCE] and colliding wind emission [CWE]) component, the Homunculus Nebula (HN), and the outer ejecta components (OE) are marked. Identified emission lines are marked by lines at their rest energies. The underlined "Fe ı" marks the location of the Fe absorption edge. The red, blue, and gray lines show, respectively, *Chandra* best-fit models of the outer ejecta (see Fig. 5), the Homunculus Nebula, and their sum, folded through the EPIC pn effective area.

4.1. *Nonvariable Components*

4.1.1. *Contribution of the Outer Ejecta and Homunculus Nebula to the X-Ray Spectra*

We use *Chandra* observations to estimate the amount of contamination from the outer ejecta and the Homunculus Nebula in the *XMM-Newton* spectra.

We extracted the spectrum of the outer ejecta from the *Chandra* CXO_{030720} HETG zeroth-order data, which has the smallest contamination from the central hard source. We extracted the source spectrum from an $83'' \times 47''$ ellipse centered on the star ("OE SRC" in Fig. 2), with its major axis parallel to the long axis of the extended outer X-ray nebula, but excluded a $20'' \times 15''$ ellipse ("HN SRC" in Fig. 2) centered on the central source and the Homunculus Nebula. We extracted background spectra from a nearby apparently source-free region. η Car is embedded in soft diffuse emission from the Carina Nebula, but its contribution to the η Car spectrum is negligible.

The spectrum from the "OE SRC" region, excluding the spectrum from the "HN SRC" region, is shown in Figure 5. This spectrum shows a strong emission line from nitrogen, which reconfirms the N enhancement in the outer ejecta found by a number of previous analyses (optical/UV, Davidson et al. 1982; X-rays, Tsuboi et al. 1997 [N/O ∼ 5]; Leutenegger et al. 2003 [N/O > 9]). This spectrum also shows a significant excess at 1.3 keV, the energy of the helium-like Mg line, which seems to require an Mg overabundance of ≳3 solar at $kT \sim 0.6$ keV (although plasma with that temperature should emit a stronger hydrogen-like Mg line). Leutenegger et al. (2003) also found a similarly strong Mg line in the *XMM-Newton* grating spectrum, although they conjectured that some of the Mg emission might be contamination from the stellar X-ray source. Our results suggest that the Mg line does in fact originate in the outer nebulosity. We modeled the extracted, background-corrected source spectrum below 3 keV (where the emission from the extended source dominates) using a simple absorbed optically thin, thermal plasma model (WABS, Morrison & McCammon 1983; MEKAL, Mewe et al. 1995), including
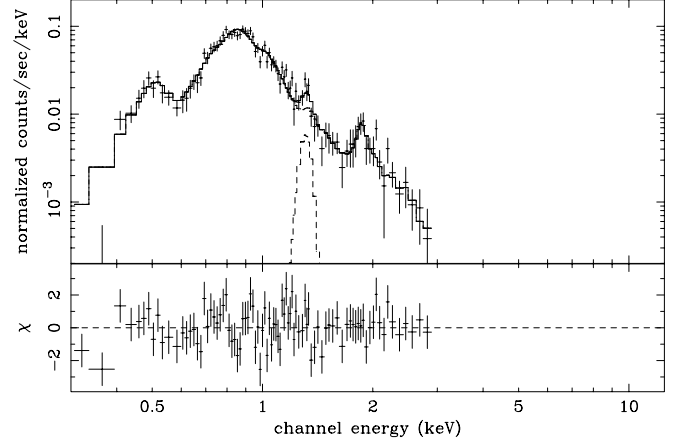

Fig. 5.—*Chandra* spectrum of the outer ejecta from CXO_{030720} (OE SRC–HN SRC in Fig. 2). The solid line shows the best-fit absorbed 1T model, and the dashed line depicts the Gaussian component for helium-like Mg.

the ACISABS[14] component to compensate for the progressive low-energy degradation of the quantum efficiency of the *Chandra* ACIS detector. We allowed the abundances to vary but constrained all abundances to have the same value except for nitrogen, which was allowed to vary independently. We added a Gaussian with a fixed line centroid at 1.31 keV with no intrinsic broadening, to account for the helium-like Mg line emission. The model successfully reproduces the spectrum of the outer ejecta, yielding a reduced χ^2 of 1.09 for 81 degrees of freedom (dof), with the best-fit parameters of $kT \sim 0.58$ keV, $N_H \sim 7.2 \times 10^{20}$ cm^{-2}, with a VMEKAL normalization of 7.2×10^{-4}, elemental abundance of ∼85 solar for nitrogen, near-solar abundance for the others, and an excess flux of ∼1.5×10^{-5} counts cm^{-2} s^{-1} for Mg. The plasma temperature, ∼0.6 keV, mainly constrained by continuum above 1 keV, agrees well with the highest plasma temperature derived from the emission lines in the *XMM-Newton* grating spectrum (Leutenegger et al. 2003). However, the N_H is smaller than interstellar absorption to η Car (≳3×10^{21} cm^{-2}; see § 2.2 of Leutenegger et al. 2003), the nitrogen abundance is overestimated from earlier measurements, and the best-fit model does not reproduce the Fe L and Ne lines near 1 keV that are observed with the high-resolution grating spectrum. This is perhaps caused by assuming a simplistic one-temperature (1T) model for a spectrum that may have multiple cooler plasma components. Therefore, this model reproduces CCD resolution spectra (≳100 eV at 1 keV) at energies above ∼0.4 keV but not higher resolution grating spectra.

The reflected X-ray emission from the Homunculus Nebula did not vary significantly between CXO_{030720} and CXO_{030828}, an interval of 40 days (Corcoran et al. 2004). Since this emission represents the accumulated X-rays reflected from the entire Homunculus Nebula, any time variation of the central source shorter than the average light-travel time from the star to the reflecting site inside the Homunculus Nebula (∼88 days) will be smeared out. We assume that the emission from the Homunculus Nebula did not vary between CXO_{030720} and CXO_{030828}, which includes all *XMM-Newton* observations during the 2003 minimum (XMM_{030722}–XMM_{030818}). To show the relative magnitude of the contamination from this reflected component, in Figure 4 we include a model fit of the *Chandra* spectrum of the reflected X-rays from the Homunculus Nebula, which we extracted from a
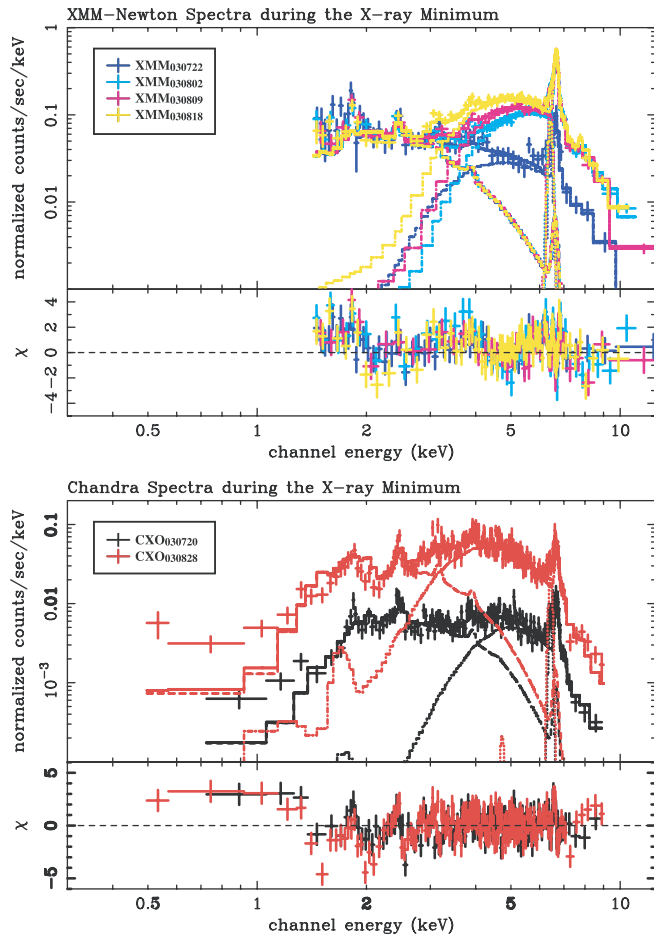
---

[14] See http://cxc.harvard.edu/cont-soft/software/ACISABS.1.1.html.

FIG. 6.—*Top*: *XMM-Newton* EPIC pn spectra during the 2003 minimum (XMM_{030722}–XMM_{030818}) after subtracting emission from the outer ejecta and Homunculus Nebula. *Bottom*: *Chandra* spectra of the central region in CXO_{030720} (*black*; HETG zeroth order) and CXO_{030828} (*red*; ACIS-S). The solid lines show the best-fit model of a simultaneous fitting of *XMM-Newton* (pn and MOS) and *Chandra* spectra by an individually absorbed 2T model. Dashed, dot-dashed, and dotted lines show the CCE component, variable component, and a Gaussian for the Fe K fluorescence line, respectively.

$20'' \times 15''$ ellipse centered on the star (HN SRC in Fig. 2), excluding a $2.5''$ radius circle (CS SRC).

Although the X-ray intensity of the Homunculus in observations outside the 2003 minimum is less certain, at these times the X-ray emission from the central source was so bright that the X-ray contamination from the Homunculus is ≲1% even if the reflected emission from the Homunculus brightened by a factor of ~3.

4.1.2. *Discovery of a "Constant" Component near the Central Source*

Figure 4 depicts the *XMM-Newton* EPIC pn spectra recorded through 2003, along with the best-fit spectral models of the outer ejecta, the X-ray Homunculus Nebula, and their sum. Except for the excess below 1 keV, which is produced by the poor absolute flux calibration of the EPIC pn,[15] the excess over the summed spectrum represents emission in a region (CS SRC in Fig. 2) within $2.5''$ of the hard X-ray peak. Apparent in Figure 4 is an excess over the model in the energy range 1–3 keV. This emission apparently did not vary in time with the harder emission and had the same flux in the *Chandra* spectra of the central region in ob-

[15] See the *XMM-Newton* calibration report CAL-TN-0018-2-3.

servations CXO_{030720}, CXO_{030828}, and CXO_{030926} (see also Fig. 6), so that the emission was securely constant for more than 2 months between 2003 July 20 and September 26. We call this component the CCE.

The CCE shows lines of helium-like S and Si ions but no lines of hydrogen-like S and Si ions. This indicates that the CCE comes from relatively cool plasma. To estimate the emission parameters of the CCE, we subtracted contributions of the outer ejecta and Homunculus Nebula from both the pn and MOS spectra (see the top panel of Fig. 6, which shows the pn spectra). We ignored data bins below 1.4 keV, where the MOS and pn spectra have significant discrepancies due to problems with the relative flux calibrations between the two instruments. To better estimate the spectrum at low energies, we also fit the *Chandra* spectra of the central region from CXO_{030720} and CXO_{030828} (see the bottom panel of Fig. 6). Because of the finer spatial resolution of *Chandra*, these spectra are mostly free from contamination by emission from the outer ejecta. Each *XMM-Newton* and *Chandra* spectrum was fitted by a combination of a low- and high-temperature, optically thin thermal plasma models with independent absorbing columns for each component, including a Gaussian line to account for the fluorescent iron line at 6.4 keV. The low-temperature component accounts for the emission from the CCE.

The parameters of the low-temperature component were tied among all the spectra, and we assumed fixed solar abundances for all elements except for silicon and sulfur, whose abundances were allowed to vary simultaneously for all the spectra. We allowed the parameters of the hard component (which represents the variable emission of the stellar source) to vary among all the spectra, but we kept the abundances at the same (nonsolar) values in each spectrum. Table 3 shows the best-fit parameters for the constant component. The spectrum can be fitted with $kT \sim$ 1.1 keV, $N_H \sim 5.0 \times 10^{22}$ cm^{-2}, with an absorption-corrected luminosity of $\log L_X \sim 34$ ergs s^{-1}, and low abundances for Si (~0.21 solar) and S (~0.47 solar).

The model, however, was not accepted at above 90% confidence for the following reasons: (1) The *Chandra* spectra show significant excess below ~1 keV, perhaps originating in foreground emission from the outer ejecta "bridge" (Weis et al. 2004; see also Fig. 2). The excess can be reproduced by including some flux from the outer ejecta using the model derived in § 4.1.1. This slightly improves the reduced χ^2 from 1.51 for 1205 dof to 1.50 for 1203 dof. The included flux is ~0.4% of the whole outer ejecta emission. (2) The model overestimates the spectra near 2 and 2.7 keV, where lines of hydrogen-like Si and S ions are, and the model underestimates the spectra near 1.8 and 2.5 keV, where lines of helium-like Si and S ions are. This suggests that the constant

TABLE 3
BEST-FIT PARAMETERS OF THE CCE COMPONENT

Parameters	1T Fit
kT (keV)	1.05 (0.96–1.13)
Z(Si) ($Z_\odot$)	0.22 (0.14–0.29)
Z(S) ($Z_\odot$)	0.47 (0.39–0.55)
EM (10^{56} cm^{-3})	7.0 (6.0–8.2)
N_H (10^{22} cm^{-2})....................	4.96 (4.77–5.16)
L_X[a] (10^{34} ergs s^{-1})..............	1.3
χ^2/dof	1.51
dof	1205

NOTE.—Elemental abundances of the hard component were found to be nonsolar but do not vary with observation.
[a] Absorption-corrected X-ray luminosity between 0.5 and 10 keV, assuming the distance of 2.3 kpc.
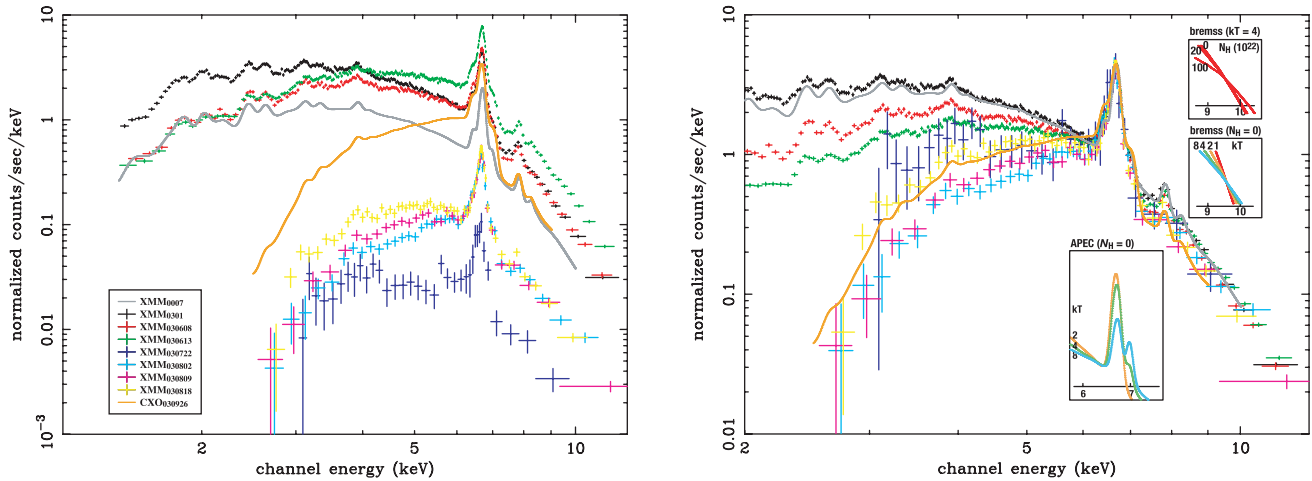
Fig. 7.—*Left*: *XMM-Newton* spectra of the variable emission. *Right*: *XMM-Newton* spectra renormalized to the line intensity of the helium-like Fe line. Best-fit models of the variable emission in XMM_{0007} and CXO_{030926}, convolved with the EPIC pn effective area, are also displayed in gray and orange. Each color represents the same observation as in Fig. 4. Boxes in the bottom panel show the high-energy slopes of the bremsstrahlung emission at $kT = 4$ keV with $N_H = (0, 2, 10) \times 10^{23}$ cm^{-2} (*top*), the bremsstrahlung emission at $kT = 1, 2, 4$, and 8 keV without absorption (*middle*), and Fe line profile of the APEC model at $kT = 2, 4$, and 8 keV with abundance of 0.5 solar (*bottom*).

component includes plasma with temperature cooler than $kT \sim 1$ keV, although an inconsistency near 2 keV between *XMM-Newton* and *Chandra* spectra could also be caused by calibration uncertainties of the *Chandra* effective area around the iridium M edge. Since cooler plasmas have lower emissivities in those lines, our simple 1T model fitting for the CCE component can underestimate the elemental Si and S abundances. (3) The model underestimates the *XMM-Newton* spectra near 3–4 keV, possibly because the variable component is a multiple-temperature plasma (see § 4.2.2). (4) The Fe K line profile is complex and cannot be fitted by a simple 1T equilibrium model (see § 4.2.3). Nevertheless, the parameters given in Table 3 should approximate the physical properties of the CCE, except perhaps for the elemental abundances, which are more dependent on details of the model.

As seen in Figure 6, the emission between 1 and 3 keV in CXO_{030720} comes predominantly from the CCE component. The 1–3 keV image in CXO_{030720} was apparently pointlike, which restricts the projected plasma size to within $\sim 1''$ of η Car, the width of the *Chandra* point-spread function. This is equivalent to a projected distance $\lesssim 2300$ AU at $d \sim 2.3$ kpc, suggesting that the hot gas that produces the CCE component is inside the Little Homunculus Nebula (which has a projected extent of roughly $\pm 2''$; Ishibashi et al. 2003).

4.2. *The Variable Component*

In order to determine the spectrum of the variable stellar component, we then subtracted from all the original spectra the recognized nonvariable emission components: the outer ejecta, the X-ray Homunculus Nebula, and the CCE component. The remaining emission represents the variable component associated with the stellar source and is shown in Figure 7. The left panel shows the variable component "corrected" for the constant components we identified. For comparison, we overlaid on the left panel of Figure 7 the best-fit models for the XMM_{0007} and CXO_{030926} data sets.

4.2.1. *Variation of the Overall Spectral Shape*

The right panel of Figure 7 shows the "corrected" variable components normalized at the Fe xxv line energy to highlight changes in the shape of the spectra. From XMM_{0007} to XMM_{0301} (an interval of 2.5 yr) the X-ray flux increased by a factor of 2–3

without remarkable changes in spectral shape. Four months later (observation XMM_{030608}), the X-ray emission decreased only below 5 keV. Five days later (observation XMM_{030613}), when η Car was close to the peak of the last flare before the 2003 minimum (Corcoran 2005), the hard X-rays above ~ 3 keV increased by a factor of 2. The X-ray emission dropped by almost 2 orders of magnitude by XMM_{030722}, the first observation after the 2003 minimum. In XMM_{030802}, the hard-band flux recovered by a factor of 3 without any significant change in the soft band. The hard-band flux stayed the same in XMM_{030802}, XMM_{030809}, XMM_{030818}, and CXO_{030828} (not shown), while the soft-band emission slightly increased. The *RXTE* light curves (Corcoran 2005) also show a clear transition in the flux level and hardness ratio between XMM_{030722} and XMM_{030802}. This means that the X-ray minimum has two states. By CXO_{030926}, only the hard-band flux recovered to the pre-minimum level.

The right panel in Figure 7 clearly shows that, throughout the observations, the hard-band slope above 7 keV did not change significantly, nor did the ratio of hydrogen-like to helium-like Fe ion lines. This means that the electron temperature of the hottest plasma did not change during the 2003 minimum. On the other hand, the soft-band flux relative to the hard band decreased gradually from the X-ray maximum through the minimum to the recovery. This looks like an increase of the absorption column to the X-ray plasma although the situation is somewhat more complicated, as the following sections describe. The 2003 minimum can be better described as an apparent decrease of the EM as suggested by earlier *ASCA* observations (Corcoran et al. 2000), which means that either the amount of X-ray–emitting material has declined or the amount that is visible to the observer is smaller.

4.2.2. *One-Temperature Fit of the Entire Spectrum*

To quantitatively describe the spectral shapes and compare them with earlier results obtained by *ASCA* and *BeppoSAX* (see § 5), we fit each spectrum by an absorbed 1T thermal APEC[16] model (which provided a better fit near the Fe K lines than the MEKAL model), with a Gaussian at 6.4 keV to account for the Fe K fluorescence line. The results are listed in Table 4.

---

[16] See http://cxc.harvard.edu/atomdb/.

TABLE 4

THE BEST-FIT MODELS FOR THE WHOLE SPECTRA

Observation	$\phi_{\rm orbit}$	kT (keV)	Z ($Z_\odot$)	Flux$_{6.4\,\rm keV}$ (10^{-4} counts cm^{-2} s^{-1})	$N_{\rm H}$ (10^{22} cm^{-2})	Observed Flux (10^{-11} ergs cm^{-2} s^{-1})	Reduced χ^2 (dof)
XMM$_{0007}$	0.470–0.471	4.6 (4.5–4.8)	0.67 (0.63–0.70)	0.91 (0.75–1.04)	5.1 (5.0–5.2)	6.5	2.85 (315)
XMM$_{0301}$	0.922–0.924	4.3 (4.2–4.4)	0.64 (0.62–0.65)	2.4 (2.3–2.6)	4.8 (4.7–4.9)	15.0	10.29 (249)
XMM$_{030608}$	0.988	4.5 (4.4–4.6)	0.83 (0.81–0.85)	4.1 (3.9–4.2)	7.4 (7.3–7.5)	12.8	12.77 (417)
XMM$_{030613}$	0.990	5.4 (5.4–5.5)	0.95 (0.94–0.97)	6.9 (6.7–7.1)	9.1 (9.0–9.2)	19.3	17.49 (548)
CXOXMM$_{0307}$	1.008–1.009	3.1 (2.8–3.6)	0.44 (0.37–0.53)	0.16 (0.13–0.20)	28 (25–32)	0.19	1.24 (193)
XMM$_{030802}$	1.015	3.6 (3.3–3.9)	0.64 (0.56–0.71)	0.65 (0.58–0.78)[b]	42 (39–45)	0.75	2.44 (119)
XMM$_{030809}$	1.018	2.9 (2.8–3.1)	0.64 (0.58–0.71)	0.55 (0.45–0.65)[b]	36 (34–38)	0.82	1.19 (94)
XMM$_{030818}$	1.023	2.9 (2.8–3.1)	0.58 (0.54–0.63)	0.37 (0.26–0.42)[b]	29 (27–30)	0.96	1.30 (161)
CXO$_{030828}$[a]	1.028	4.6 (3.4–5.4)	0.48 (0.37–0.60)	0.31 (0.3–0.43)	18 (17–21)	0.73	1.54 (137)
CXO$_{030926}$	1.042	2.9 (2.3–3.3)	0.40 (0.36–0.45)	3.6 (3.0–4.3)	36 (33–40)	6.6	1.40 (242)

NOTES.—These fits refer to the spectrum between 2 and 10 keV after subtraction of the CCE and the Homunculus emission. Parentheses show the range of values for which $\Delta\chi^2 = 2.7$ from the best-fit value.
[a] About 4% of the photon events are piled up, causing the spectrum to appear slightly harder.
[b] These values are upper limits since the line shapes are not clearly seen in the spectra.

Most of the fits were not acceptable at the 90% confidence level. One reason for the poor fit by the absorbed 1T models is that the strong Fe Kα profile is quite complicated, as described in § 4.2.3. Another reason, in particular for the spectra before the 2003 minimum, is that the plasma is really composed of multiple components with different temperatures, as shown by Corcoran et al. (2001b), as their best-fit plasma temperatures $kT \sim 4$–5 keV do not account for the strong lines of helium-like S and Si ions seen in the *XMM-Newton* spectra (which should be emitted from plasma with $kT \sim 1$ keV). The plasma temperatures outside the 2003 minimum ($kT \sim 4$–5 keV) are consistent with earlier results (Tsuboi et al. 1997; Corcoran et al. 2000; Viotti et al. 2002; Leutenegger et al. 2003), but they are probably overestimated by our 1T model fit (see the next section). The derived absorption column, which does not depend strongly on temperature for $kT \sim 3$–5 keV, gradually increased from $N_{\rm H} \approx 5 \times 10^{22}$ to $\approx 4 \times 10^{23}$ cm^{-2}.

4.2.3. Fits to the $E > 5$ keV Spectrum

The EPIC spectra marginally resolved emission lines below $\sim$5 keV and could not reliably measure the neighboring continuum level. Spectral modeling of this energy band with unconstrained elemental abundances, therefore, has intrinsic uncertainty.

On the other hand, the spectrum above 5 keV is relatively simple and provides an unambiguous measure of the hottest plasma from the continuum slope and Fe K line intensities. To characterize the hottest plasma, we thus fit the spectra above 5 keV by a simple absorbed 1T model.

In each observation, we simultaneously fit all the available spectra, using an APEC thermal equilibrium model for the thermal emission. We simultaneously fit the spectra of two observations, CXO$_{030720}$ and XMM$_{030722}$, which were obtained during the 2003 minimum within 2 days of each other. A preliminary fit to the bright phase spectra showed that most spectra could be fitted with $kT = 3.3$ keV and a nickel abundance near 0.8 solar, with solar abundances for other elements. Therefore, we fixed the nickel abundance at 0.8 solar and the temperature at 3.3 keV, and we varied the Fe abundance, column density, and emission measure. We included two narrow Gaussian lines to account for lines of Fe Kα and Kβ fluorescence, fixing their centroids at 6.4 and 7.1 keV, with their line widths (σ) fixed at 0.01 keV, and the Kβ line flux fixed at 11.3% of the Kα line flux. We used photoelectric absorption cross sections calculated by Balucinska-Church & McCammon (1992). Table 5 gives the best-fit parameters, and the spectra, along with their best-fit models, are shown in Figure 8. The spectra except for XMM$_{0007}$ and CXOXMM$_{0307}$

TABLE 5

THE BEST-FIT MODELS FOR THE SPECTRA ABOVE 5 keV

Observation	$\phi_{\rm orbit}$	$Z_{\rm Fe}$ ($Z_\odot$)	log EM (cm^{-3})	EW(Fe) (eV)	$N_{\rm H}$ (10^{22} cm^{-2})	Reduced χ^2 (dof)
XMM$_{0007}$	0.470–0.471	0.48 (0.45–0.52)	58.1 (58.1–58.2)	87 (62–99)	17 (14–20)	1.43 (86)
XMM$_{0301}$	0.922–0.924	0.48 (0.47–0.50)	58.5 (58.5–58.5)	99 (85–104)	17 (16–19)	4.07 (82)
XMM$_{030608}$	0.988	0.55 (0.54–0.57)	58.5 (58.5–58.5)	164 (158–172)	21 (20–22)	4.21 (154)
XMM$_{030613}$	0.990	0.44 (0.43–0.45)	58.9 (58.9–58.9)	119 (114–123)	36 (35–37)	3.66 (245)
CXOXMM$_{0307}$	1.008–1.009	0.38 (0.30–0.47)	57.0 (56.9–57.0)	∼233 (183–325)[a]	40 (32–51)	1.35 (90)
XMM$_{030802}$	1.015	0.50 (0.46–0.55)	57.7 (57.6–57.7)	≲213[a]	53 (48–58)	1.91 (71)
XMM$_{030809}$	1.018	0.70 (0.63–0.77)	57.5 (57.4–57.5)	≲257[a]	32 (26–37)	1.59 (54)
XMM$_{030818}$	1.023	0.62 (0.57–0.67)	57.5 (57.5–57.5)	≲150[a]	27 (23–30)	1.65 (84)
CXO$_{030828}$[b]	1.028	0.33 (0.24–0.42)	57.5 (57.4–57.6)	∼149 (96–214)[a]	37 (28–47)	1.81 (54)
CXO$_{030926}$	1.042	0.33 (0.29–0.37)	58.7 (58.6–58.8)	110 (90–136)	56 (50–62)	1.54 (130)

NOTES.—These fits refer to the spectrum after subtraction of the CCE and the Homunculus emission. The plasma temperature and the Ni abundance were fixed at 3.3 keV and 0.8 solar, respectively.
[a] These values are regarded as upper limits since the spectra did not clearly show the iron fluorescence line peak.
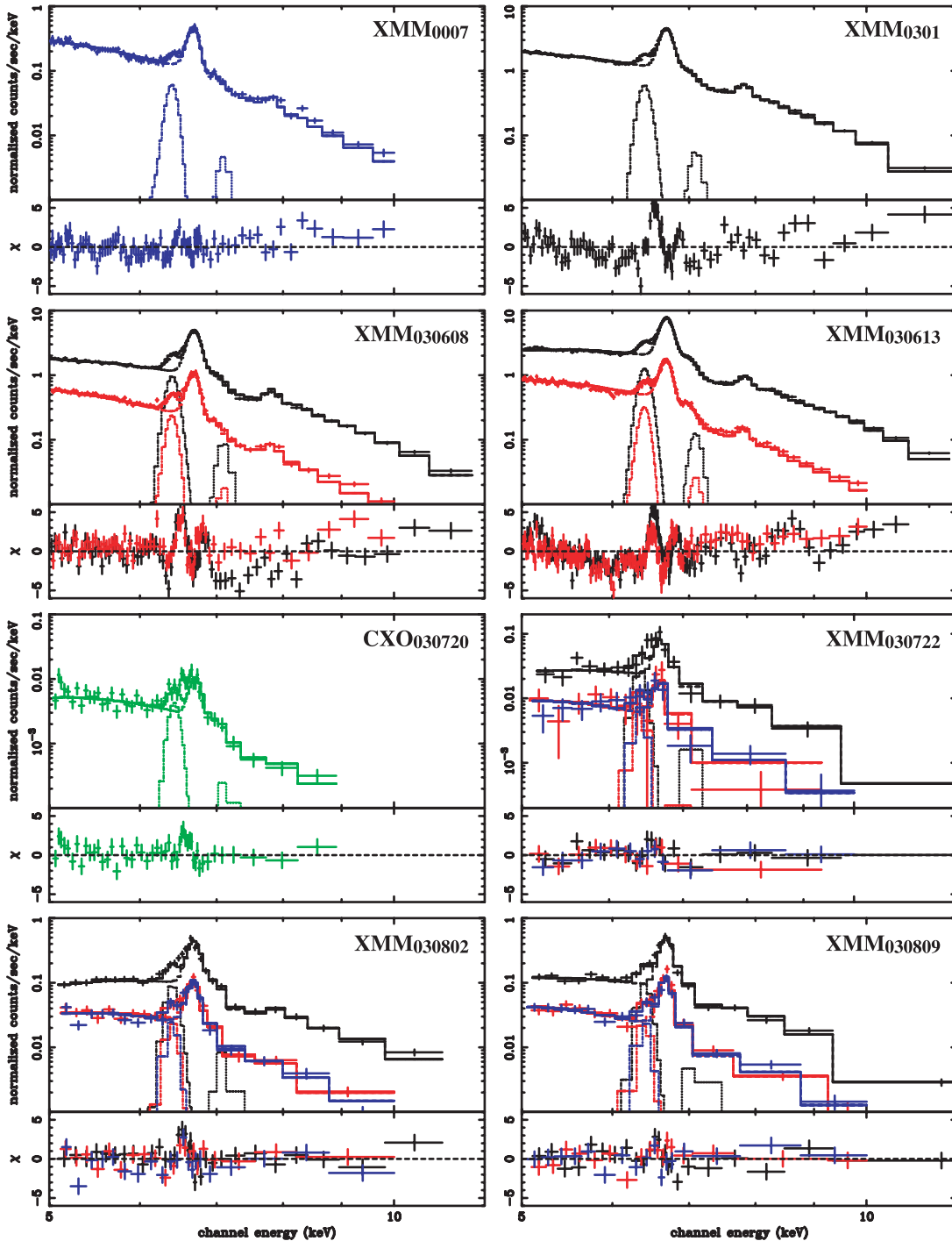[b] About 4% of the photon events pile up, causing the spectrum to be slightly hard.

Fig. 8.—Spectra above 5 keV: EPIC pn (*black*), EPIC MOS1 (*red*) and MOS2 (*blue*), ACIS (*green*), and HETG (*gray*: +first order; *brown*: −first order). The solid lines show the best-fit absorbed optically thin thermal plasma model (APEC code) with Gaussian components for Fe Kα and Kβ.

accept the assumed model at <90% confidence, mostly because these spectra show several spectral features that are not fitted by the model.

The most prominent of these features are excesses on the blue and red sides of the K-shell lines of helium-like iron. Those excesses are not caused by poor energy or gain calibration, since there is good consistency in profile between the XMM$_{030613}$ spectrum and the near-contemporaneous *Chandra* grating spectrum. The blue excess could be explained if the K lines of Fe xxv are Doppler broadened, with $\Delta v \sim 4000$ km s^{-1}. This is similar to the

derived wind velocity of the companion star, $v \approx 3000$ km s^{-1} (Pittard & Corcoran 2002). The red excess, especially during the 2003 minimum and CXOXMM$_{0307}$ and XMM$_{030802}$ when the X-ray flux was the weakest, would require an Fe xxv Doppler shift of $\Delta v \sim 7000$ km s^{-1}, and such high velocities are not expected in η Car. However, the red excess may be produced by unresolved emission lines of Fe in ionization stages below Fe xxv in the 6.5–6.6 keV band. Interestingly, the *ASCA* minimum spectrum in ASCA$_{971224}$ showed a similar excess (see § 5.2), while a *Chandra* grating spectrum near apastron ($\phi \sim 0.53$) showed a
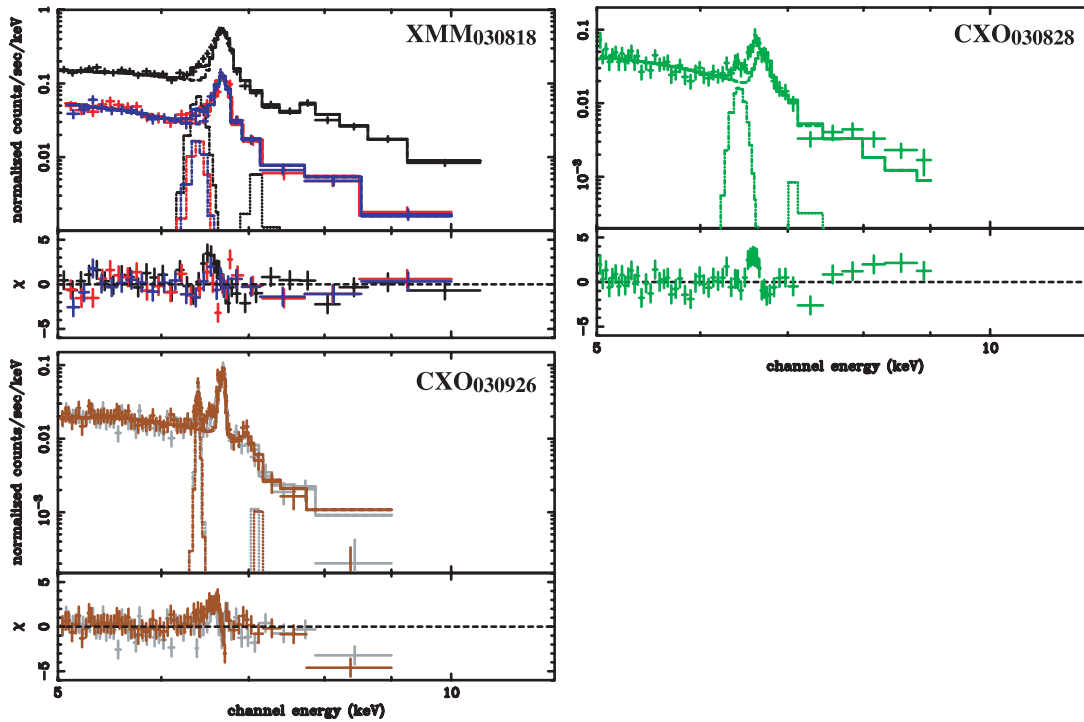
Fig. 8—*Continued*

similar broadband excess (Pittard & Corcoran 2002). The presence of lower ionization iron lines would indicate that the hottest plasma is no longer in collisional ionization equilibrium at 3.3 keV and that the electron temperature is higher than the ion temperature. Nonequilibrium ionization (NEI) effects have been claimed in the X-ray spectrum of WR 140, another colliding wind system (Pollock et al. 2005).

Similarly, a humplike spectral feature is perhaps present between 5 and 6.4 keV and becomes more noticeable during the early phase of the minima. There are no specific emission lines in this energy band, except a weak Ca XIX line at 4.56 keV. A similar feature is sometimes seen in the X-ray spectra of some active galactic nuclei (Tanaka et al. 1995), produced by gravitationally redshifted material very near the central black hole. However, there is little evidence that η Car houses a black hole because of the lack of short-term X-ray variability and relatively low X-ray luminosity.

A second feature is a hard "tail" at $\gtrsim 9$ keV, best seen in the residuals in XMM_{0007}, XMM_{0301}, XMM_{030608}, and XMM_{030613} (see Fig. 8). This feature is probably not an instrumental or background artifact: none of the spectra (except for CXO_{030828}) suffer photon pileup, and source count rates are much higher than the background. During the 2003 minimum the tail seems weaker or nonexistent, although this may simply be an artifact since the source is weak at these times. The slope above 9 keV in XMM_{030613} can be fitted by a bremsstrahlung model with $kT \sim 10$ keV or a power-law model with $\Gamma \sim 2.3$. Viotti et al. (2004) measured a similar photon index for a hard tail extending up to 150 keV, seen in a *BeppoSAX* PDS spectrum in 2000 June ($\phi \sim 0.46$), but the flux between 13 and 20 keV, 1.4×10^{-11} ergs cm^{-2} s^{-1}, is about 3 times larger than the extrapolation of the hard tail we measured in XMM_{030613}. The hard excess we see in the *XMM-Newton* data may be from an extremely hot plasma in the colliding wind region, or from nonthermal emission due to first-order Fermi acceleration at the wind contact surface, which would produce a population of relativistic electrons that can upscatter UV photons

from the stellar photosphere and/or X-ray photons from the wind-wind shock.

We also clearly see an excess at ~ 8.5 keV in the pn spectra in observations XMM_{0301} and XMM_{030613}. This feature might be due to emission from K-shell lines of heavy metals like Cu and Zn. Although the EPIC instrumental background shows emission from those elements (Strüder et al. 2001), inspection of the EPIC background data provided by the XMM project showed that the instrumental background at this energy was negligible in spectra obtained outside the minimum. This feature could indicate an overabundance of Cu or Zn or perhaps be a part of the Cu edge at ~ 9 keV (which would also require a large Cu overabundance). On the other hand, the feature might be produced by absorption edges from Fe XXV (~ 8.8 keV) and Fe XXVI at ~ 9.3 keV (Lotz 1967).

Finally, the fourth feature is a marginal dip around 7 keV, which is seen in all the pn spectra, but which is not so prominent in the MOS spectra. This dip could be caused by an underestimate of the line intensity of hydrogen-like Fe ions at 6.9 keV (perhaps due to an underestimate of the maximum plasma temperature) or an underestimate of the strength of the Fe edge structure at 7.1 keV, perhaps indicating larger Fe absorption. This dip is especially noticeable in the observation CXO_{030926} and will be discussed more fully in the analysis of our *Chandra* HETGS observations (M. F. Corcoran et al. 2007, in preparation).

4.2.4. *Adding a Soft Component to Reproduce the Entire Spectrum*

Extrapolation of the model spectrum above 5 keV from the XMM_{0007}, XMM_{0301}, XMM_{030608}, XMM_{030613}, CXO_{030828}, and CXO_{030926} data to lower energies underestimates the observed emission at $E < 5$ keV, indicating the presence of additional cooler emitting material. We thus modeled the emission below 5 keV by fixing the best-fit model spectrum derived in § 4.2.3 and adding another 1T component with independent absorption. The results are given in Table 6 and Figure 9.

TABLE 6
ADDITIONAL SOFT COMPONENT FOR THE SPECTRUM BELOW 5 keV

Observation	ϕ_{orbit}	kT (keV)	Z ($Z_\odot$)	log EM (cm^{-3})	N_H (10^{22} cm^{-2})	Reduced χ^2 (dof)
XMM$_{0007}$........................	0.470−0.471	1.1 (1.1−1.2)	0.25 (0.20−0.31)	58.3 (58.2−58.4)	5.4 (5.2−5.5)	2.04 (225)
XMM$_{0301}$........................	0.922−0.924	1.1 (1.1−1.1)	0.18 (0.16−0.19)	58.8 (58.8−58.8)	5.4 (5.3−5.4)	8.85 (164)
XMM$_{030608}$.....................	0.988	1.1 (1.1−1.1)	0.24 (0.22−0.26)	58.6 (58.6−58.7)	6.9 (6.8−7.0)	5.41 (260)
XMM$_{030613}$.....................	0.990	1.6 (1.5−1.6)	0.25 (0.22−0.28)	58.6 (58.5−58.6)	7.7 (7.5−7.8)	12.02 (300)
CXO$_{030828}$	1.028	0.5 (0.4−0.9)	<0.58	59.9 (58.1−60.1)	29 (17−39)	1.32 (80)
CXO$_{030926}$	1.042	0.9 (0.6−1.8)	0.28 (0.05−0.75)	59.2 (58.0−60.5)	23 (13−33)	0.52 (109)

NOTE.—These fits refer to the spectrum after subtraction of the CCE and the Homunculus emission.

These fits were not accepted at >90% confidence except the fit to the CXO$_{030926}$ spectra. One reason for the poor quality of the fits is that the fixed hard component, which reproduces emission above 5 keV, somewhat overestimates the emission near 5 keV, which might indicate that we slightly underestimated the absorption to the hard component. Another reason is that the best-fit models do not reproduce the strengths or locations of many emission lines, in particular S XIV, which is generally emitted by plasma at $kT > 1$ keV. This means that the spectra may require additional components with kT between 1 and 3 keV. The N_H values we derive from this two-component modeling are very close to the ones from the 1T fitting in § 4.2.2.

5. COMPARISON WITH THE PREVIOUS OBSERVATIONS NEAR X-RAY MINIMA

The weekly to daily monitoring of η Car with *RXTE* (Corcoran 2005) showed significant cycle-to-cycle variability in flux and X-ray hardness. Since the *RXTE* data are contaminated by instrumental and cosmic background, we compared our *XMM-Newton* and *Chandra* results with earlier spatially resolved observations
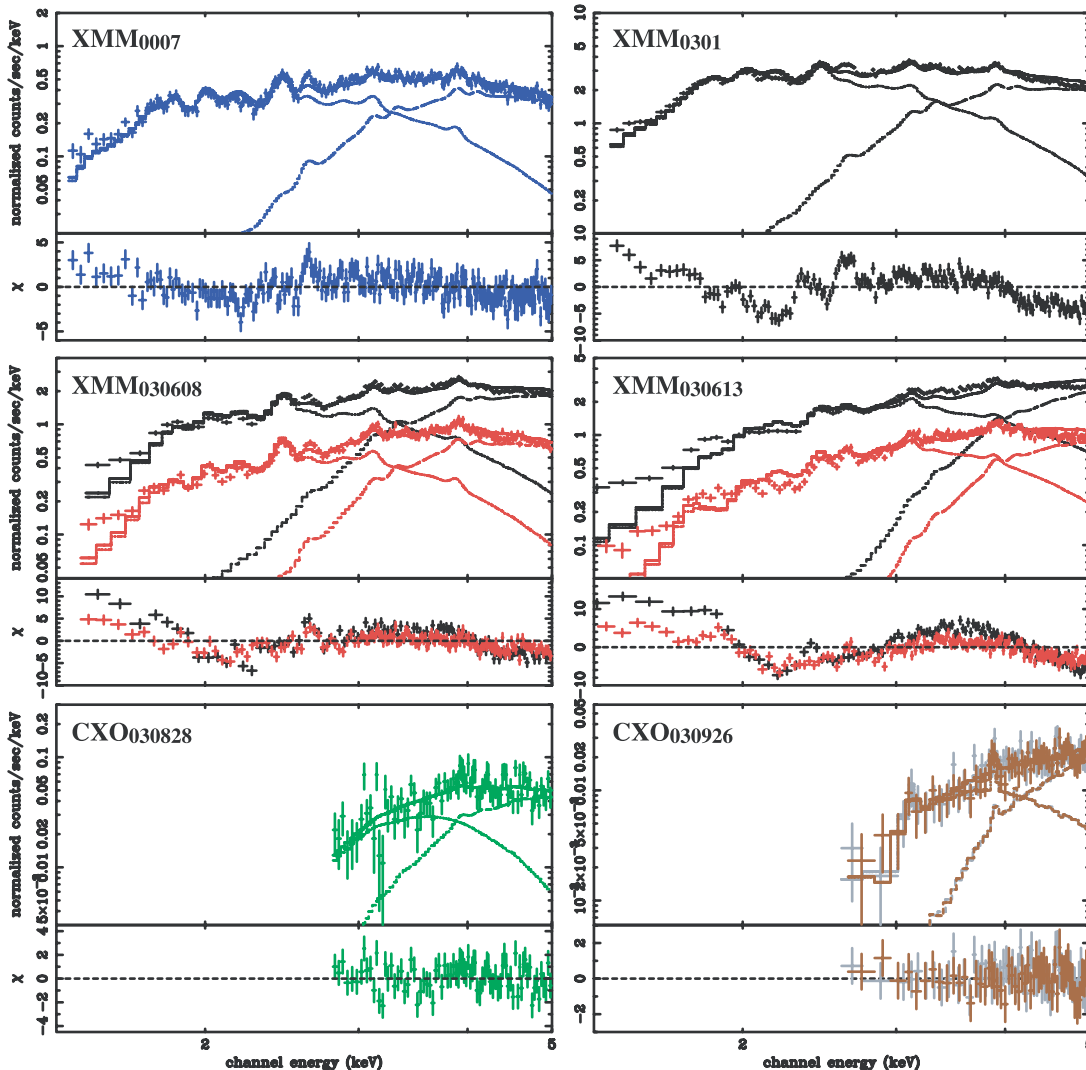

FIG. 9.—Fits of the spectra below 5 keV.

TABLE 7
Observations around the Minimum from Previous Cycles

Abbreviation	Satellite	Date	P_{orbit}	Exposure (ks)	N_{H} (10^{22} cm^{-2})	kT (keV)	References
ROSAT$_{920612}$	*ROSAT*	1992 Jun 12, 22:33	-0.998	23.6	...	...	
ASCA$_{970703}$	*ASCA*	1997 Jul 3, 09:58	-0.082	12.6	4.16±0.23	3.79±0.31	1
ASCA$_{970719}$	*ASCA*	1997 Jul 19, 15:11	-0.074	12.8	4.09±0.30	4.12±0.39	1
ASCA$_{971224}$	*ASCA*	1997 Dec 24, 09:29	0.004	58.8	...	...	1
SAX$_{980318}$	*BeppoSAX*	1998 Mar 18, 05:01	0.045	39.0[a]	15.4±0.4	4.35±0.15	2
ASCA$_{980716}$	*ASCA*	1998 Jul 16, 04:40	0.104	13.4	5.00±0.52	4.89±0.88	1

Note.—N_{H} and kT refer to the hottest components in two-temperature fits of the entire spectra; *ASCA* results refer to analysis of the GIS2 spectra.
[a] Exposure time for the MECS23 detector.
References.—(1) Corcoran et al. 2000; (2) Viotti et al. 2002.

from *ASCA* (Tanaka et al. 1994), *BeppoSAX* (Scarsi 1993), and *ROSAT* (Trümper 1984).

Between phase $-0.10 \lesssim \phi_{\mathrm{orbit}} \lesssim 0.10$, there were four *ASCA* observations and one *BeppoSAX* observation near the 1998 minimum and one *ROSAT* observation during the 1992 minimum. These observations are summarized in Table 7. Because of the extended point responses (FWHM of roughly a few arcminutes) of *ASCA* and *BeppoSAX* compared to *XMM-Newton*, source spectra extracted from these observations used relatively large ($\sim 3'$) extraction regions (Corcoran et al. 2000; Viotti et al. 2002). This extraction area is a factor of ~ 20 larger than the area used in the *XMM-Newton* analysis (XMM SRC) and a factor of ~ 5000 larger than the area used in the *Chandra* analysis (CS SRC). Because the neighborhood of η Car is crowded with X-ray sources and diffuse emission, the *ASCA* and *BeppoSAX* spectra will suffer greater contamination from neighboring sources.

5.1. Comparison of the 1997/1998 and 2003 Spectra outside the Minimum

Outside the minimum, contamination of the stellar source spectra in the *ASCA* and *BeppoSAX* observations from the surrounding sources, the CCE component, and the reflection from the Homunculus Nebula is $\lesssim 10\%$ above ~ 2.5 keV (see § 5.2).

Viotti et al. (2002) tried two models to fit their *BeppoSAX* spectra: an absorbed single-temperature bremsstrahlung model plus Gaussian for the spectrum between 3 and 10 keV, and an ab-

sorbed two-temperature (2T) model to fit the entire spectrum between ~ 0.1 and 10 keV. Both gave consistent results with each other for the central hard variable component. On the other hand, in an analysis of *ASCA* spectra obtained just prior to the 1997/ 1998 minimum, Corcoran et al. (2000) fixed the emission from the outer ejecta using the model derived in Corcoran et al. (1998). Although the coolest temperature they used to fit the *ASCA* spectra ($kT \sim 0.3$ keV) is a bit lower than our adopted temperature ($kT \sim 0.6$ keV) and the resulting difference in the outer ejecta flux is about a factor of 3 at ~ 2 keV, this only produces a $\sim 1\%$ uncertainty in the flux of the variable emission outside the 2003 minimum. The results of their *BeppoSAX* and *ASCA* analyses, therefore, are comparable to the result we derived from our 1T fits to the entire *XMM-Newton* and *Chandra* spectra in § 4.2.2.

The plasma temperatures in the 1997/1998 observations were always around ~ 4–5 keV, which is similar to our results. The derived values of N_{H} varied significantly with phase (Fig. 10), reaching a maximum during the X-ray minimum and declining thereafter. The variation in 2003 was similar to the N_{H} variation in 1997/1998, except for the interval just at the end of the minimum. Although *BeppoSAX* and *Chandra* observed η Car at a similar orbital phase ($\phi_{\mathrm{SAX\,980318}} \sim 0.045$, $\phi_{\mathrm{CXO\,030926}} \sim 1.042$), the N_{H} measured with *Chandra* in 2003 is a factor of 2 larger than the value derived by Viotti et al. (2002) from the *BeppoSAX* observations in 1998. This is consistent with the behavior of the hardness ratio after the recovery as measured by *RXTE*, which
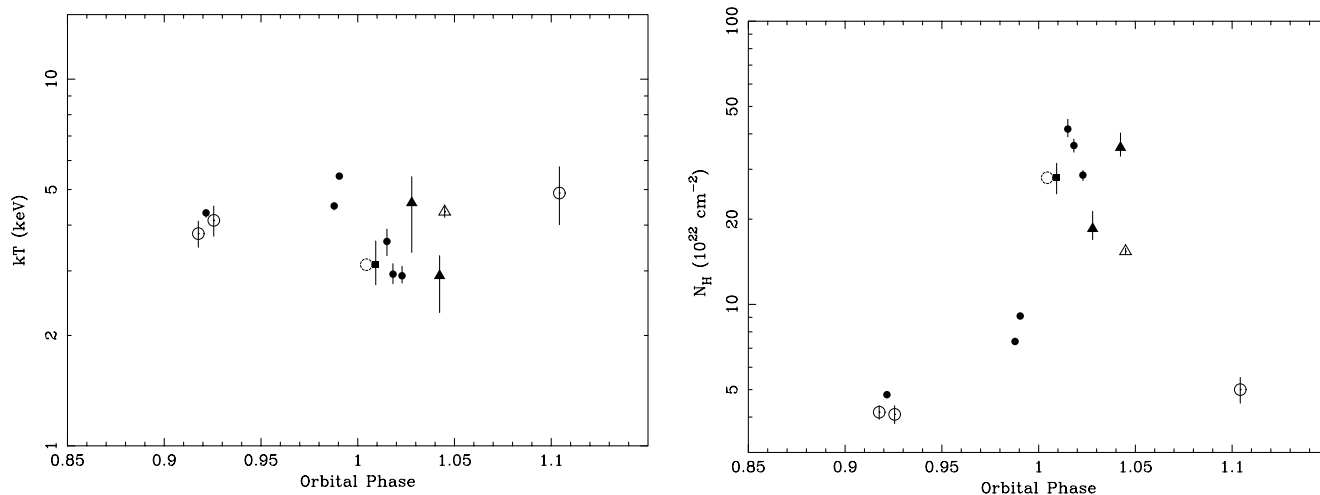

Fig. 10.—Variation of the temperature and absorption column (N_{H}[whole]) vs. orbital phase. The filled symbols are from the 2003 cycle (*circles*: *XMM-Newton*; *triangles*: *Chandra*; *squares*: simultaneous fit between *XMM-Newton* and *Chandra*). The open symbols are from the 1997/1998 cycle (*circles*: *ASCA*; *triangle*: *BeppoSAX*). The *ASCA* spectrum during the 2003 minimum at phase 1.004 is consistent with the N_{H} and kT values from CXOXMM$_{0307}$, as shown by the dashed circles.

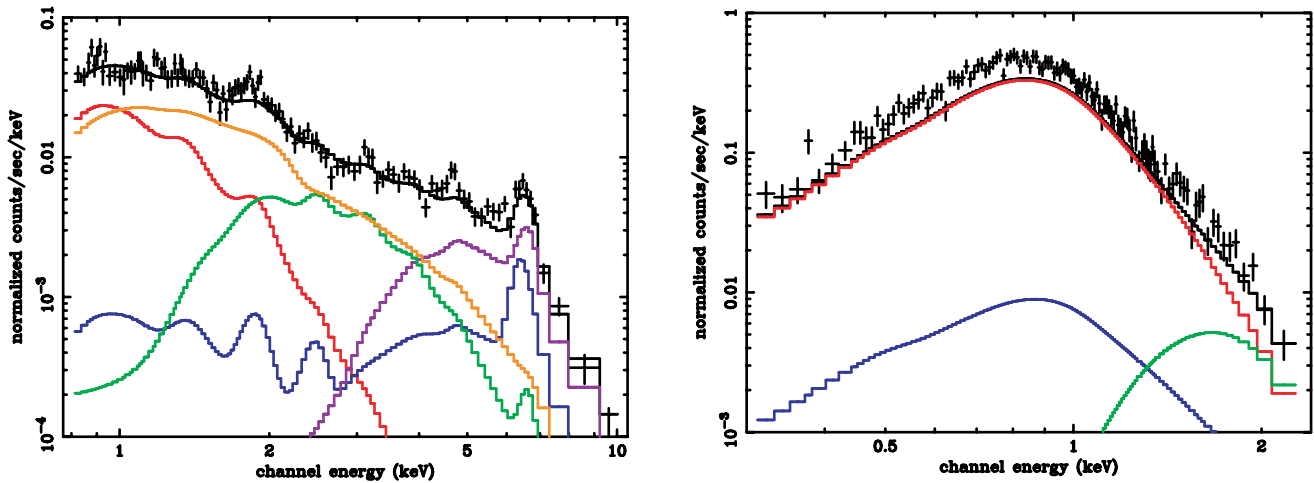Fig. 11.—*Left*: *ASCA* GIS2+3 spectrum on 1997 December 24. *Right*: *ROSAT* PSPC spectrum on 1992 June 12. In each plot the spectrum around η Car during the X-ray minimum in 2003 is shown (*red*: the outer ejecta; *blue*: X-ray Homunculus Nebula; *green*: CCE component; *purple*: variable emission in CXOXMM$_{0307}$; *orange*: surrounding sources within 3′). The solid black line shows the sum of these emission components.

was higher in the 2003 recovery than in the 1998 recovery (Corcoran 2005).

5.2. *Comparison of the 1997/1998 and 2003 Spectra during the Minima*

In order to compare this data set with the X-ray observations during the 2003 minimum, we reanalyzed the ASCA$_{971224}$ GIS data. We screened the "revision2" data taken from the HEASARC archive[17] using `gisclean` and filtered it with the standard criteria, which excludes data affected by the South Atlantic Anomaly, Earth occultation, and high background in regions with low geomagnetic rigidities. For both GIS2 and GIS3 detectors, we used a 3′ radius circle centered on η Car as the source region "3′ SRC" and used as background emission from a 3′ radius circle designated "3′ BGD" centered to the northeast of η Car (Fig. 2) where the soft diffuse X-ray emission from the Carina Nebula is apparently weak (Hamaguchi et al. 2007). We used the standard GIS response files, version 4.0 (g[23]v4_0.rmf), and generated ancillary response functions with ASCAARF version 3.10. We then merged both GIS2 and GIS3 spectra together to improve the signal-to-noise ratio. The left panel of Figure 11 shows the GIS spectrum from ASCA$_{971224}$.

Because the stellar source was faint during the minimum and the *ASCA* point-spread function is large, contamination by nearby X-ray sources is significant for this observation. We therefore tried to estimate the contamination from emission from sources within 3′ of η Car 3′ SRC using XMM$_{030722}$ (when the central point source of η Car was the weakest) excluding the source region XMM SRC used for the analysis of η Car from the *XMM-Newton* MOS2 data. We used the same background region as we used to estimate the *ASCA* background emission (3′ BGD). About 10% of the emission from η Car (which amounts to $\sim$20% of the emission from the surrounding sources even in XMM$_{030722}$) contaminates the 3′ SRC region. We simulated the contamination due to η Car and subtracted it from the *XMM-Newton* source spectrum. The subtracted spectrum (Fig. 12) does not show any evidence of the extremely strong nitrogen line at $\sim$0.5 keV from the outer ejecta, suggesting that contamination is well removed.

The resulting *XMM-Newton* spectrum, after subtracting the simulated η Car spectrum, shows weak emission lines at $\sim$0.9 and 1 keV from Ne IX and Ne X, $\sim$0.8 keV possibly from Fe, and a mar-

[17] See http://heasarc.gsfc.nasa.gov/W3Browse/.

ginal excess around $\sim$3–4 keV from Ca. This spectrum can be fitted either by an optically thin, thermal (MEKAL) model with 2T components or by a cool component plus a power-law component for the hard emission at slightly below the 90% confidence, assuming common absorption for both components (Table 8). In either model, the average absorption to these sources is consistent with the interstellar value ($\sim$3 $\times$ 10^{21} cm^{-2}; see § 2.2 of Leutenegger et al. 2003). As the spectrum does not have strong emission lines, the elemental abundance of the 2T model is small ($\sim$0.04 solar), while the abundances are not constrained by the 1T plus power-law model. We thus fixed the abundances at 0.3 solar, a typical value for stellar X-ray emission obtained from low-resolution CCD spectra (e.g., OB stars, Kitamoto & Mukai 1996; Kitamoto et al. 2000; low-mass main-sequence stars, Tagliaferri et al. 1997; low-mass pre–main-sequences stars, Yamauchi et al. 1996; Kamata et al. 1997; Tsuboi et al. 1998).[18] The observed flux is $\sim$3.2 $\times$ 10^{-12} ergs cm^{-2} s^{-1} (0.5–10 keV).

[18] High-resolution grating spectra with *Chandra* and *XMM-Newton* showed complex line profiles especially from OB stars, and therefore the abundance obtained from low-resolution spectra may not reflect real elemental abundance (e.g., Cassinelli et al. 2001; Kahn et al. 2001; Miller et al. 2002).
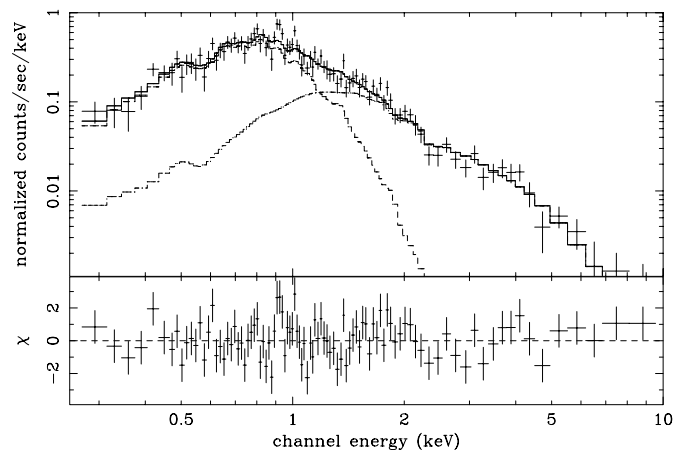

Fig. 12.—*XMM-Newton* MOS2 spectrum from XMM$_{030722}$ extracted from a 3′ radius circle excluding emission from η Car. The solid line shows the best-fit 2T MEKAL model with common absorption, while the dashed lines show the individual fit components.

TABLE 8
The Spectral Fit of the Surrounding Region

| | Soft Component | | Hard Component | | | | | |
Model	kT (keV)	log EM (cm^{-3})	kT (keV)	log EM (cm^{-3})	Γ	Z ($10^{-1}\,Z_\odot$)	$N_{\rm H}$ (10^{21} cm^{-2})	Reduced χ^2 (dof)
2T	0.24 (0.18–0.29)	57.7 (57.2–58.5)	2.6 (1.9–3.3)	56.2 (56.2–56.4)	...	0.36 (0.19–0.70)[a]	3.6 (2.6–5.5)	1.28 (92)
1T+pl	0.27 (0.23–0.30)	56.5 (56.3–56.8)	...	...	2.5 (2.4–2.7)	3 (fix)[b]	2.6 (2.1–3.3)	1.26 (93)

Note.—Values in parentheses denote 90% confidence limits.
[a] The abundance parameters of both soft and hard components are tied together.
[b] The absorption is insensitive to abundance in the range between 0 and 10 $Z_\odot$.

The $3'$ SRC region includes at least 55 *Chandra* X-ray point sources (Evans et al. 2003): 6 OB stars and 49 unidentified, weak sources that might be low-mass pre–main-sequence stars. The combined absorption-corrected flux from these sources calculated from Tables 3 and 4 in Evans et al. (2003) is 1.3×10^{-12} ergs cm^{-2} s^{-1} (0.5–2.04 keV). There is also diffuse emission within the source region that is also calculated from Evans et al. (2003) to have a flux of $\sim 5.7 \times 10^{-12}$ ergs cm^{-2} s^{-1}. The total absorption-corrected flux, $\sim 7 \times 10^{-12}$ ergs cm^{-2} s^{-1}, is roughly consistent with our result 8.2×10^{-12} ergs cm^{-2} s^{-1} (0.5–2.04 keV, unabsorbed). Moreover, the combined absorption-corrected fluxes of the point sources are as large as the flux from the hard component (1.7×10^{-12} ergs cm^{-2} s^{-1}), and the flux from the diffuse emission is as large as the soft component, 6.5×10^{-12} ergs cm^{-2} s^{-1}, in the 0.5–2.0 keV band. As seen in Figure 2, many point sources are detectable at intermediate energies, where the hard component is dominant, but they are not clear in the soft band (except for HDE 303308). The hard component probably represents emission from point sources with the soft component dominated by diffuse emission and HDE 303308.

We have compared the *ASCA* spectrum to a model derived from our fits to the *Chandra* and *XMM-Newton* spectra including emission from the outer ejecta, from the Homunculus Nebula, from the CCE component and the variable model that fits the spectrum obtained from the CXOXMM$_{0307}$ observation, along with emission from the surrounding sources (diffuse emission and point sources) that fall within the $3'$ extraction circle. The *ASCA* spectrum agrees well with this combined model. Assuming that emission from the outer ejecta, X-ray Homunculus Nebula, and the surrounding sources did not vary between 1997 and 2003 and that spectral shapes of the CCE and variable components did not change dramatically, the fluxes of both CCE and variable components are the same within 50% in 1998 as in 2003.

5.3. *Comparison with the 1992 Minimum*

There is one *ROSAT* PSPC observation of η Car during the minimum in mid-1992. Corcoran et al. (1995) used this observation to show that the X-ray emission in the hard *ROSAT* band ($E > 1.6$ keV) decreased by a factor of 2 at that time. *ROSAT*, however, had very little effective area above 2 keV so that the bulk of the variable emission was not observable by *ROSAT*.

Corcoran et al. (1995) extracted a spectrum from a $1.85'$ radius circle excluding a $30''$ radius circle around the nearby bright star HDE 303308. To minimize contamination from surrounding sources, we reextracted the spectrum using an elliptical source region of $65'' \times 47.5''$, which includes emission from the outer ejecta but excludes HDE 303308 and point and diffuse sources around η Car. We took the same background region as used in our analysis of ASCA$_{971224}$. In analyzing the PSPC spectrum, we used the standard response file pspcb_gain2_256.rmf from the *ROSAT* calibration database, but we generated the ancillary re-

sponse file using the PCARF version 2.1.3 in FTOOLS as appropriate for this observation.

The PSPC spectrum is shown in the right panel of Figure 11. We have overlaid all the spectral components of η Car on this spectrum as we did for the ASCA$_{971224}$ spectrum, except for the component due to the surrounding sources, whose contribution would be small in the *ROSAT* spectrum due to the smaller PSPC extraction region. Emission between 0.5 and 1 keV, where the outer ejecta component is dominant, is about a factor of 30% larger than the model. This difference may be due to calibration uncertainties between *ROSAT* and *XMM-Newton*, or it might be produced by another variable source within the *ROSAT* extraction area. Although the *XMM-Newton* model of the CCE component only contributes to the few highest channels of the PSPC detector, this component is consistent with the *ROSAT* spectrum. Thus, it appears that *ROSAT* did not detect the stellar component at all during the 1992 minimum.

6. DISCUSSION

6.1. *Emission from the Variable Component*

RXTE clearly showed that the variable emission is periodic and leaves little doubt that the emission is produced by the WWC in a binary system (Corcoran 2005) and, if so, that the X-ray minimum occurs near periastron passage. Our results further strengthen this conclusion. The temperature of the hottest plasma, ~ 3 keV, was mostly unchanged through the cycle, consistent with the collision of stellar winds at terminal velocities (see, e.g., Ishibashi et al. 1999). Furthermore, the spectral shape varied in a periodic way, as well. However, the $N_{\rm H}$ measured just after the end of the X-ray minimum was about a factor of 2 larger during the 2003 cycle than it was during the 1998 cycle.

Most of the light curves derived from the *Chandra* and *XMM-Newton* data showed no short-term variations, suggesting that the X-ray plasma is produced by a steady source and is probably larger than $V_{\rm shock}t_{\rm exp}$, where $V_{\rm shock}$ is the preshock velocity and $t_{\rm exp}$ is the exposure time of the observation. For $V_{\rm shock} \sim 3000$ km s^{-1} (corresponding to shock temperatures of ~ 3–4 keV) and exposure times of ~ 10 ks (corresponding roughly to the *XMM-Newton* observing time), the size of the emitting region is probably $\gtrsim 0.2$ AU and perhaps considerably larger. The *RXTE* light curve also shows clear variations in observations separated by as little as 1 day, suggesting that the size of the emitting region is 0.2 AU $\lesssim r \lesssim 2$ AU. Although the orbital elements are currently uncertain, the stellar separation at periastron may be as little as 1.5 AU (Corcoran et al. 2001a), so that the size of the emitting region may be comparable to the stellar separation at periastron passage.

Spectra outside the 2003 minimum require at least two temperatures, $kT \sim 3$ and 1–1.5 keV, consistent with the analysis of a *Chandra* grating spectrum by Corcoran et al. (2001b). The failure
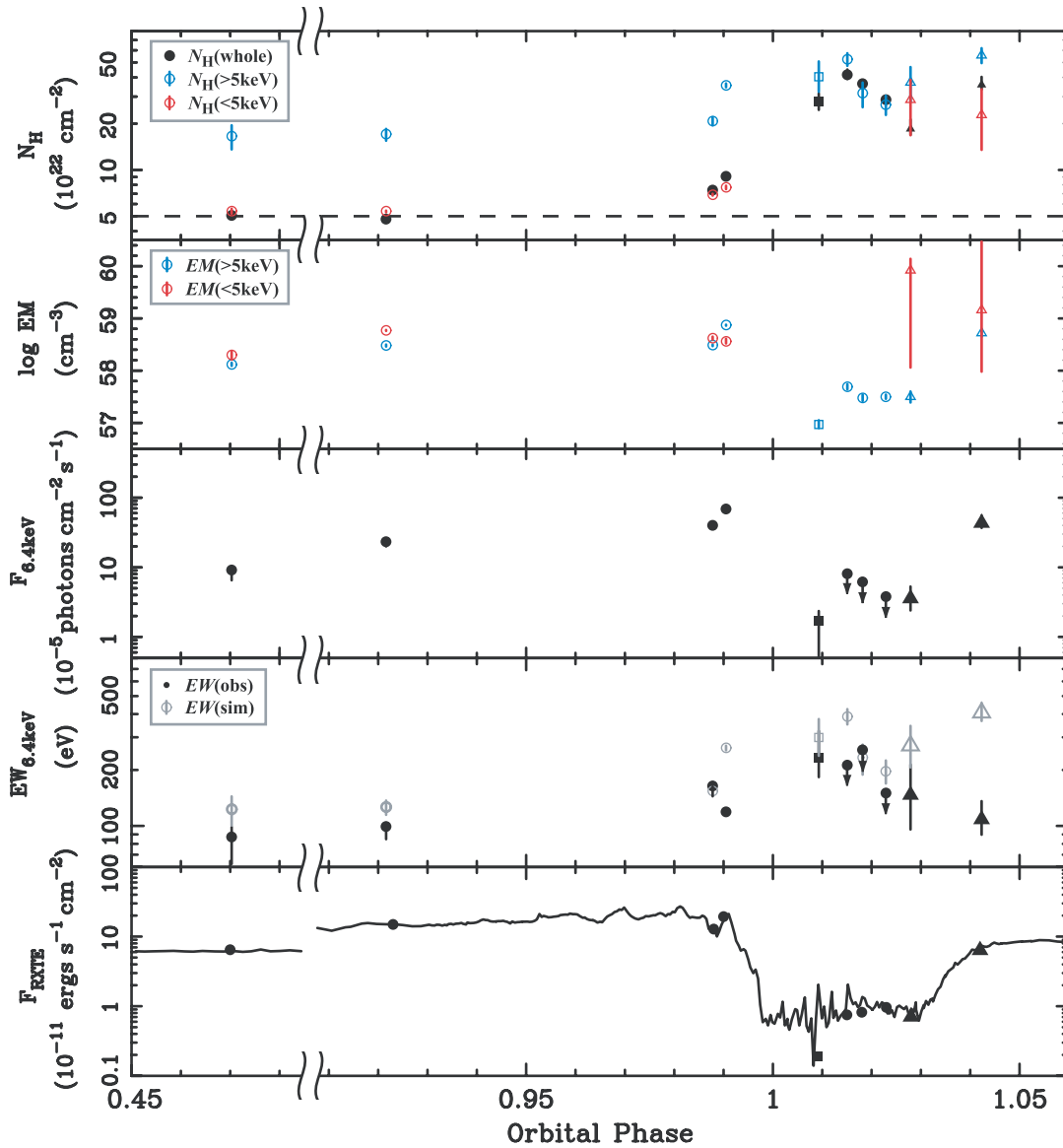
FIG. 13.—Variation of N_H, EM, intensity, and EW of the Fe fluorescence line and *RXTE* flux in the 2003 cycle. The *XMM-Newton* results are shown as circles, *Chandra* results as triangles, while squares show results derived from a simultaneous fit between *XMM-Newton* and *Chandra*. The dashed line in the top panel represents our estimate of the absorption beyond the central source.

to fit most of the spectra by 2T models in § 4.2.4 is perhaps an indication of the presence of more than two temperatures. This is consistent with a hydrodynamic simulation of the WWC plasma (Pittard & Stevens 1997), in which the plasma temperature is the highest near the stagnation point where the winds collide head-on and cooler farther along the bow shock. The excess at the blue side of the Fe xxv line discussed in § 4.2.3 may represent streams from the stagnation point flowing outward near the companion's wind terminal velocity.

The *RXTE* light curves also displayed quasi-periodic X-ray "flares," which correspond to hardness ratio maxima (Corcoran et al. 1997; Corcoran 2005). XMM$_{030608}$ occurred near the bottom of one of these flares, while XMM$_{030613}$ occurred near a flare peak. A comparison of these spectra in Figure 7 shows that the hard-band flux went up by a factor of 2, while the soft-band flux below ~3 keV did not change except that emission lines are apparently weaker in XMM$_{030613}$. This is consistent with an increase of the hardness ratio measured with *RXTE*. This indicates

a slight increase in kT and/or EM for the hottest plasma, possibly caused by increase of the density of the high-temperature gas near the stagnation point, as discussed for a similar event in the previous cycle observed with *ASCA* (Corcoran et al. 2000). The emission at $E \lesssim 3$ keV, on the other hand, did not vary strongly between those observations. One possibility is that hard X-ray emission from the highest temperature plasma at the stagnation point of the shock cone varied strongly due to density fluctuations of the primary or secondary wind, with the soft X-ray emission coming from a larger area that averages out such fluctuations. Another possibility is that the flares are related to instabilities in the WWC plasma.

6.2. *The Absorber around the WWC Plasma*

Before the 2003 minimum, N_H measured from our fits to the spectra above 5 keV (hereafter $N_H[>5$ keV$]$) was always about a factor of 4 larger than N_H measured from the spectra below 5 keV ($N_H[<5$ keV$]$; Fig. 13). $N_H[>5$ keV$]$ mainly represents Fe
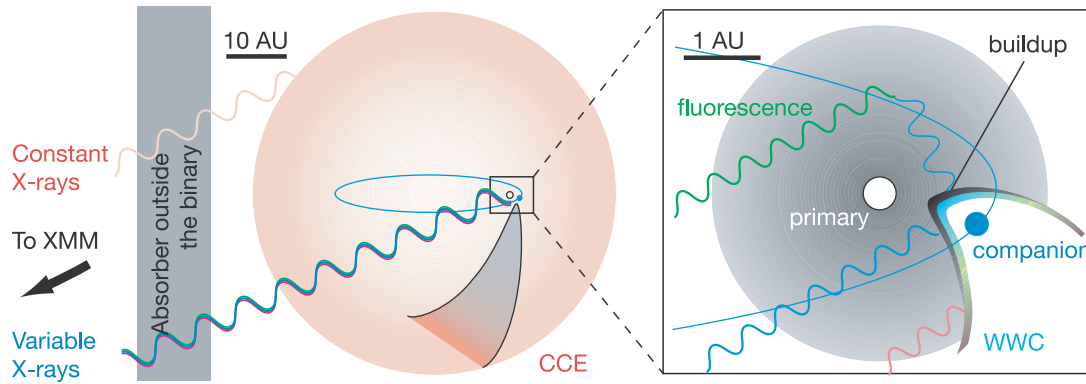
Fig. 14.—Cartoon of the η Car system. Winds from the primary star and the companion collide together, to form the WWC region, which has a conical shape. Behind the WWC boundary is a low-density region filled with the wind of the companion star. The apex where the winds collide head-on has hotter gas than the downstream material and also accumulates a buildup of cool primary wind material in front. We view the X-ray emission from the WWC plasma through the cool material at the apex and/or the undisturbed primary wind and the absorber that lies far outside the binary system. Iron K fluorescence emission is produced by scattering in the primary wind. One possibility for the CCE, where the CCE is produced in outer shock, is shown. Emission from the CCE only passes through the outer absorber beyond the binary system.

absorption, while $N_H[<5 \text{ keV}]$ represents absorption by lighter elements (Morrison & McCammon 1983). Although this discrepancy can be produced by an Fe overabundance in the η Car ejecta, the elemental abundances around the stellar source are near solar except for He and N, which are overabundant, and O and C, which are strongly depleted (Hillier et al. 2001; Verner et al. 2005; Davidson et al. 1984). Abundance anomalies of He, N, O, and C would not change the amount of absorption above ~ 1 keV. This means that the soft emission does not suffer as strong absorption as the hard emission before the minimum, and hence this supports the idea that the variable emission originates in multiple-temperature plasmas with various absorptions. This is consistent with the idea that the hot emission originates from a highly absorbed region near the apex of the shock cone, with the lower energy emission arising from a region farther along the shock interface that suffers less absorption. Neither $N_H[>5 \text{ keV}]$ nor $N_H[<5 \text{ keV}]$ varied significantly between XMM_{0007} at $\phi \sim 0.47$ (close to apastron) and XMM_{0301} at $\phi \sim 0.92$, when the stellar separation changed by about a factor of 3. The value of $N_H[<5 \text{ keV}]$ before the minimum ($\sim 5 \times 10^{22}$ cm^{-2}) may be absorption beyond the wind of the primary. The higher value of $N_H[>5 \text{ keV}]$ suggests that extra absorbing material must be located near the hottest plasma.

After XMM_{0301} and through the onset of the 2003 minimum, $N_H[>5 \text{ keV}]$ and the absorption column derived from fitting the spectra over the entire 1–10 keV band ($N_H[\text{whole}]$; see Fig. 10) increased to $(3–5) \times 10^{23}$ cm^{-2}. As shown in Figure 10, the observed maximum column density occurred near the midpoint of the X-ray minimum, and the column densities declined thereafter toward the end of the minimum. During the X-ray minimum, $N_H[<5 \text{ keV}]$ was unmeasurable because of the near total suppression of the low-energy flux. This could mean that the EM of the cool component decreased during the minimum, or that the absorption to the cool plasma also increased on the line of sight. Nevertheless, the $N_H[>5 \text{ keV}]$ confirms that the X-ray minimum is closely associated with an increase in the amount of absorption along the line of sight. This suggests that the WWC plasma entered into, or was hidden behind, the densest part of wind from the primary star. The behavior of the absorption toward the hard component, $N_H[>5 \text{ keV}]$, is in interesting contrast to the behavior of $N_H[\text{whole}]$. $N_H[>5 \text{ keV}]$ had already increased to $\sim 4 \times 10^{23}$ cm^{-2} by XMM_{030613} (i.e., prior to the start of the X-ray minimum), and it did not change strongly after that. This could be explained if the WWC region was bent, perhaps by the

Coriolis force, causing the stagnation point to enter into the densest part of the primary's wind earlier than the downstream material.

The column density did not decline until some time after the 2003 minimum ended. This confirms that the column density variation is not completely synchronous with the X-ray minimum. Conjunction probably occurred during the interval when N_H was near its maximum observed value, in the phase interval $0.99 < \phi < 1.05$. We note that the N_H measured in 2003 ($\phi = 1.042$) is a factor of 2 larger than the N_H measured in 1998 ($\phi = 0.045$). Davidson et al. (2005, see their Fig. 2c) also noted that the absorption component in the Paη ($\lambda 9017$) line in 2003.72 ($\phi \approx 1.0$) was stronger than in 1998.21 ($\phi \approx 0.0$), which might also indicate that the amount of absorbing material in the line of sight near the start of the X-ray minimum is increasing with time. However, they also note that the equivalent widths of the Hα emission lines were lower just after the end of the 2003 minimum. This might suggest a distribution of wind material that has preferentially grown denser in the line of sight than perpendicular to the line of sight in the 1998–2003 interval.

The equivalent width (EW) of the Fe K fluorescence line varied between 100 and 200 eV, which is far smaller than the EW (~ 1.5 keV) produced by scattering X-rays from the Homunculus Nebula (Corcoran et al. 2004). This suggests that the X-ray emission in all the observations comes directly from the WWC plasma, even during the X-ray minimum, with only a small scattered component (see Fig. 14). From Inoue (1985) the Fe K fluorescence line EW produced by scattering from a spherically symmetric medium around an X-ray source is EW $\sim 7.5 N_H[>5 \text{ keV}]/10^{22}$ eV, where we have multiplied Inoue's coefficient by 0.75, the flux ratio in the 7.1–9 keV band between a $kT \sim 3.3$ keV thermal emission component appropriate to the η Car spectra and the $\Gamma = 1.1$ power-law emission component assumed by Inoue (1985). In Figure 13 we plot the expected Fe K fluorescence line EWs as open symbols for a spherically symmetric scattering medium. The differences between the expected and observed equivalent widths seem to be larger when the X-ray flux goes up and smaller when it goes down (XMM_{030608}, XMM_{030613}, and CXO_{030926}), which may suggest that the variation of the fluorescence line is delayed by light-travel time.

The observed EWs are $\sim 25\%$ smaller than the expected EWs even during the XMM_{0007} ($\phi = 0.470$) and XMM_{0301} ($\phi = 0.923$) observations when the direct X-ray emission did not vary strongly. This suggests that the scattering material is not spherically

symmetric as assumed in Inoue (1985) and that there is a deficit of scattering material off the line of sight. This deficit is probably produced by the WWC, since the region on the companion side of the shock has a much lower density than on the primary star's side. In order to reduce the fluorescent Fe emission by 25%, the full opening angle of the wind shock cone would need to be $\sim120°$. This is consistent with the measurement of the half-opening angle of $50°–120°$ by Pittard & Corcoran (2002).

6.3. The Nature of the X-Ray Minimum

The 2003 X-ray minimum can be described as an apparent decrease in EM, along with an increase in N_H. However, a column density of $N_H \sim 5 \times 10^{24}$ cm^{-2} is needed to reduce the emission at 10 keV by 2 orders of magnitudes, and the observed maximum column density ($N_H \sim 5 \times 10^{23}$ cm^{-2}) is much lower than this. The $ASCA$ observations during the 1997/1998 minimum (Corcoran et al. 2000) also appeared consistent with an apparent decline in EM.

Two mechanisms could produce the observed decrease in EM. One possibility is an "eclipse model," namely, that the emitting region is almost totally, but not completely, obscured by an optically thick absorber with $N_H \gtrsim 10^{25}$ cm^{-2}, and we only see the least absorbed residual emission during the minimum. Ishibashi et al. (1999) and Corcoran et al. (2001a) tested the eclipse model using the $RXTE$ light curve of η Car and showed that the duration of the X-ray minimum (~3 months) at high energies ($E > 5$ keV) was difficult to explain for a spherically symmetric wind from η Car if the mass-loss rate was constant at $\sim10^{-4}\,M_\odot$ yr^{-1}. The eclipse model seems to require that the wind is not spherically symmetric, or that the absorption to the hard X-ray–emitting region was enhanced for an extended interval near periastron passage. It also suggests that a portion of the hard emission is visible during the minimum so that the size of the hottest region is greater than the size of the occulting region.

Another possibility is that the emissivity of the WWC itself fades during the minimum, i.e., that there is a decline in the amount of material hot enough to generate ~5 keV X-rays. Some WWC models predict a change in the X-ray emissivity of the shock around periastron. For example, "radiative braking" (Gayley et al. 1997), in which UV photons from η Car decelerate the companion's wind at phases near periastron, could reduce the intrinsic X-ray emission from the WWC at $E > 5$ keV. Davidson (2002) suggested that strong instabilities near periastron might cause the shocked gas to radiatively cool, reducing the emission at high energies. Soker (2005) and Akashi et al. (2006) suggested that Bondi-Hoyle accretion of the primary star's wind by the companion star near periastron could suppress the companion's wind and thus reduce the emission from the colliding wind shock for a brief period. In optical observations, the He II $\lambda4687$ emission line, which is believed to arise near the WWC shock, decreased in concert with the X-ray drop (Steiner & Damineli 2004). Martin et al. (2006) argued that the disappearance of this line in a direct view of the star and in a reflected polar view (the so-called FOS4 position; Stahl et al. 2005) indicated a waning of the shocked gas during the minimum.

Below we examine some of the behaviors of the electron temperature, iron line profile, iron fluorescence line variation, and lack of variation at $E > 7$ keV during the minimum from the 2003 X-ray spectra to try to decide between these two mechanisms.

6.3.1. Electron Temperature

The electron temperature of the hottest material did not change significantly during the 2003 minimum, as the normalized spectra at the bottom of Figure 7 clearly show. The constancy of the elec-

tron temperature of the hottest material argues against radiative braking, shock instability, or accretion models that predict that the plasma temperature should decrease. The Akashi et al. (2006) model in particular predicts complete shutdown of the WWC activity during periastron passage and therefore could only be consistent with a constant electron temperature if an alternative X-ray emission mechanism during the minimum could produce plasma at nearly the same temperature as the WWC emission. If the shock actually disappears during the minimum, then the constancy of the high-energy X-ray continuum requires that a small part of the 3000 km s^{-1} secondary wind continues to produce a shock by encountering material directly at normal incidence.

6.3.2. The Iron Line Profile

The variable excess emission on the red side of the Fe xxv line can be explained by NEI effects in the high-temperature plasma, and variations in the strength of this feature mean that the ion temperature of some of the high-temperature plasma in the colliding wind shock changed during the minimum. This might favor mechanisms in which the intrinsic emission from the shock declines with time near periastron, although the NEI effect itself does not reduce emissivity of the continuum. The observed excess at ~6.55 keV is consistent with emission lines of Fe xxi, present at an ionization timescale $\tau = nt \sim 10^{10}–10^{11}$ s cm^{-3} in the ~3.3 keV plasma, where n is the gas density and t is the time after the gas starts heating. Since the gas density $n \propto D^{-2}$, τ should be larger by more than 2 orders of magnitude at periastron than at apastron (using the orbital elements of Corcoran et al. 2001a). Thus, near periastron the plasma should reach ionization equilibrium much faster (~15 minutes; Soker 2005) than at apastron. Perhaps near periastron, both the cooling timescale and the equilibrium timescale decrease relative to their values at apastron, but the cooling timescale decreases faster. This means that near periastron the fraction of nonequilibrium gas to gas in equilibrium is larger than it is near apastron. However, since the radiative cooling timescale has the same dependence on gas density as the ionization equilibrium timescale ($\propto n^{-1}$), an additional cooling mechanism (such as adiabatic expansion or conduction) needs to be effective near periastron in order to decrease the cooling timescale faster than the equilibrium timescale.

6.3.3. Iron Fluorescence Line Variations

As noted in the previous section, the EWs of the Fe K fluorescence line stayed below ~200 eV during the 2003 minimum, and therefore the observed X-ray emission is direct emission, with only a small scattered component. The Fe fluorescence line flux decreased by a factor of ~50 during the 2003 minimum (Fig. 13). This could be produced by reducing the number of $E > 7.1$ keV X-ray photons from the source seen by the fluorescing region, or by reducing the number of photons from the fluorescing region that reach the observer. If we assume that the fluorescing region extends far from the stars, then during the 2003 minimum either the X-ray source is nearly entirely covered by obscuring material along the line of sight to the fluorescing region, or the intrinsic X-ray emissivity has declined so that fewer ionizing photons reach the fluorescing medium. This picture is consistent with a similar variation of He II $\lambda4687$ emission between the direct emission from the central WWC region and polar emission scattered from the southeastern lobe (Stahl et al. 2005; Martin et al. 2006).

6.3.4. The Lack of Variation at $E > 7$ keV during the Minimum

The hard-band X-ray emission above ~7 keV reached its lowest value after the 2003 minimum started, recovered by a factor

of 3 after XMM$_{030722}$, and did not vary for at least $\sim$3 weeks from XMM$_{030802}$ to CXO$_{030828}$. Since *RXTE* light curves showed a similar trend in the previous cycle, the time variation seems to be phase repeatable. The observed X-ray flux after XMM$_{030722}$ was $\sim$5% of the flux at XMM$_{030613}$. It is very difficult for an eclipse of the X-ray–emitting region by an opaque disk (e.g., similar to that proposed by Ishibashi et al. 1999) to keep the observed flux constant for so long a time, since the stellar motion would be so fast near periastron that the emitting region moves beyond the occulter on $\sim$day timescales, causing a short eclipse and a rapid rise in X-ray brightness. Perhaps a ''leaky absorber'' eclipse, in which the absorbing medium is very extended and composed of optically thick clumps, could better describe the behavior of the observed flux during the minimum. Models in which the shock cools may not be consistent with the constancy of the $E > 7$ keV emission either, unless some residual emission at high energies could be generated after the shock cools.

6.4. *The Origin of the CCE Component*

The CCE component did not vary within the 2 months during the 2003 minimum when it could be observed. It apparently had the same spectrum during the 1998 minimum (as shown by our analysis of ASCA$_{971224}$) and did not show any enhanced emission during the minimum in 1992. This suggests that the X-ray source is stable on timescales of 5–10 yr. The *Chandra* image during the 2003 minimum restricts the size of the emitting plasma to $\lesssim 1''$, constraining the maximum size of the CCE at $\lesssim 2000$ AU. The column density to this component, $N_H \sim 5 \times 10^{22}$ cm^{-2}, is smaller than the column density to the variable emission component around the 2003 minimum, but each component shows nearly the same column density in 2003 January (before the 2003 minimum) and near apastron. After correcting for absorption, the X-ray luminosity of the CCE is $\sim 10^{34}$ ergs s^{-1}. This suggests that a stable luminous source is present outside of the absorbing material that lies in front of the colliding wind source at periastron.

One possibility is that the CCE component is produced within the wind of the companion star and/or η Car due to the inherent instabilities of their radiatively driven winds. The X-ray properties of the CCE component, $kT \sim 1$ keV with little apparent X-ray variation, resemble the X-ray properties of normal OB stars (e.g., Berghöfer et al. 1997; Corcoran et al. 1993). For OB stars $\log(L_X/L_{bol}) \approx -6$ to -8 (Berghöfer et al. 1997), so that the X-ray luminosity of the CCE corresponds to a bolometric luminosity $L_{bol} \sim 10^{40}$–10^{42} ergs s^{-1}. This is somewhat larger than the luminosity of the companion according to Verner et al. (2005) ($L_{bol} \sim 4 \times 10^{39}$ ergs s^{-1}), but near the luminosity of η Car ($L_{bol} \sim 2 \times 10^{40}$ ergs s^{-1}; Hillier et al. 2001).

Alternatively, the CCE emission could be produced in ambient gas shocked by a strong outflow from the stellar winds (see Fig. 14). The maximum size of the CCE ($r \lesssim 2000$ AU) means that it is inside the Little Homunculus Nebula (Ishibashi et al. 2003), so that the CCE component might be produced by the collision of the polar wind from η Car with the Little Homunculus. The velocity of the polar wind from η Car is believed to be $v \sim 1000$ km s^{-1} (Smith et al. 2003a), which is sufficient to heat gas to $kT \sim 1$ keV. If all the kinetic energy of this outflow is converted to thermal energy, the required mass-loss rate would have to be only $\sim 3 \times 10^{-8}$ $M_\odot$ yr^{-1} in order to match the observed emission measure ($\sim 7.0 \times 10^{56}$ cm^{-3}), which is only 3×10^{-4} to 3×10^{-5} of the mass-loss rate of η Car ($\sim 10^{-3}$ to 10^{-4} $M_\odot$ yr^{-1}; Hillier et al. 2001; Pittard & Corcoran 2002). The gas density inside the shell structure of the Little Homunculus should be less than the density of the shell, which is 10^6 cm$^{-3} < n_H < 10^7$ cm^{-3}

(Ishibashi et al. 2003). Assuming that radiative cooling dominates, the cooling timescale of the plasma is $\tau \sim 3nkT/n^2\Lambda(T)$, where $\Lambda(T)$ is the emissivity. With a plasma density of $n < 10^7$ cm^{-3}, plasma temperature $kT \sim 1$ keV, and $\Lambda(1$ keV$) \sim 3.1 \times 10^{-23}$ ergs s^{-1} cm^3, then $\tau > 0.5$ yr, consistent with our result.

A third alternative is that the CCE might be associated with the outflowing material from the WWC that collides with cold circumstellar gas and is reheated. The required mass-loss rate streaming out through the WWC is given by $\dot{M} = 2L_X/\epsilon V^2 \sim 10^{-8}/[\epsilon(V/2000$ km s$^{-1})^2]$ $M_\odot$ yr^{-1}, where ϵ is the efficiency to convert the kinetic energy to X-ray emission and V is the velocity of the outflow, which should be $\gtrsim 1000$ km s^{-1} from the CCE temperature. Since most of the companion's wind goes into the shock cone, the $\dot{M}$ of the outflowing material should be $\sim 10^{-5}$ $M_\odot$ yr^{-1} (Pittard & Corcoran 2002), and ϵ should only be $\sim 0.1\%$.

7. CONCLUSIONS AND SUMMARY

We have observed η Car at key phases around the X-ray minimum in 2003 using the *XMM-Newton* and *Chandra* satellites and studied the variation of the X-ray spectral shape. We also compared the behavior of the X-ray emission during the 2003 minimum with observations during earlier minima made by *ASCA*, *BeppoSAX*, and *ROSAT*. The results are summarized as follows:

1. During the minimum, the hard- and medium-band emission from the central point source decreased to 1%–5% of the flux outside the minimum, but the emission did not disappear. The X-ray flux varied in an apparently stepwise way near the middle of the minimum, suggesting that the X-ray minimum has two states. The light curve within any single observation did not show significant variability on timescales of a few kiloseconds, supporting the idea that the hard X-ray emission is produced in a WWC.

2. The spectrum of the variable emission component changed markedly throughout the X-ray minimum. The medium-band emission decreased gradually relative to the hard emission. Assuming an absorbed 1T model for the entire spectrum, the absorption to the central source increased from 5×10^{22} to 4×10^{23} cm^{-2}. The hard-band flux went up prior to the X-ray minimum and decreased abruptly during the 2003 minimum, without changing the spectral slope significantly, suggesting that the plasma electron temperature is constant around 3 keV.

3. The line flux ratios between the helium-like ions and hydrogen-like ions of Si, S, and Fe seen in the spectra before the 2003 minimum indicate a similar type of multitemperature plasma as seen near apastron by Corcoran et al. (2001b).

4. The values of N_H derived from the spectra above 5 keV ($N_H[>5$ keV$]$) are larger than those values of N_H derived from the entire spectra (N_H[whole]) or from the spectra below 5 keV ($N_H[<5$ keV$]$) but show less variation than N_H[whole] or $N_H[<5$ keV$]$. This suggests that the hotter plasma has stronger absorption; i.e., emission from η Car is multitemperature, and each emission component is associated with an independent absorption component. This means that the hotter and cooler emissions originate in spatially distinct regions. The hardest emission, which is believed to arise from material near the stagnation point of the WWC region, perhaps shows the effects of a buildup of material as the colliding wind shock plows through the primary wind.

5. The Fe xxv line profile showed a small blue excess, as well as a strong red excess before the 2003 minimum. The blue excess may be due to Doppler shifting of the line centroid or line broadening, and if so, the observed velocity is $\sim$4000 km s^{-1}. The red excess may indicate that some of the plasma is no longer in ionization equilibrium. The line showed a stronger red excess during

the 2003 minimum than outside the minimum, which we interpret as a decrease in the cooling timescale of the plasma near periastron. Interestingly, we note that an outburst spectrum of the dwarf nova SS Cyg taken with the *Suzaku* satellite showed a similar red excess on the Fe K line profile accompanied with a decrease in the hard-band X-ray flux (M. Ishida et al. 2007, in preparation).

6. We find evidence for a hard tail at $E > 9$ keV, at about an order of magnitude larger than the background level, in spectra outside the X-ray minimum. This indicates either the presence of very hot plasma in the system or nonthermal emission perhaps produced by first-order Fermi acceleration of particles, which then Compton upscatter UV seed photons from the stellar photospheres and/or X-ray photons from the shock.

7. The values of N_H and kT of the X-ray spectrum at corresponding phases in previous cycles are very similar to those during the 2003 cycle, except during the recovery phase. In particular, the *ASCA* spectrum during the 1997/1998 minimum ($ASCA_{971224}$) is almost identical to the spectrum from $CXOXMM_{0307}$. The difference in N_H during the recovery, as measured by *Chandra* and *BeppoSAX*, could be produced by an increase in the density of the wind from η Car.

8. The EWs of the Fe fluorescence line at 6.4 keV are always below the values expected from $N_H[>5 \text{ keV}]$ assuming a spherically symmetric absorber. This is probably because the absorber is not spherically symmetric and is consistent with the lack of scattering matter in the lower density wind of the companion if the full opening angle of the shock cone is $\sim 120°$, consistent with the value derived by Pittard & Corcoran (2002).

9. The X-ray minimum is caused by the apparent decrease of the plasma EM. An eclipse model seems to explain the observed constancy of the plasma electron temperature, while the small EWs of the Fe fluorescence line and the deformation of the Fe xxv He-like triplet might indicate a real decline in the amount of hot gas in the colliding wind shock. It might also indicate that nearly all of the shock is hidden by an optically thick but slightly porous stellar wind.

10. We discovered a central constant emission (CCE) component very near the central X-ray source. The CCE component can be seen between 1 and 3 keV during the X-ray minimum; at other times the emission from the colliding wind source overwhelms it. This component showed no variation on either short timescales within any observation or between observations for about 2 months during the 2003 minimum, and it was apparently the same during the 1997/1998 and 1992 minima. The CCE spectrum exhibited emission lines of Si xiii and S xiv and can be fitted by an absorbed 1T model with $N_H \sim 5 \times 10^{22}$ cm^{-2}, $kT \sim 1.1$ keV, and absorption-corrected $L_X \sim 10^{34}$ ergs s^{-1}. *Chandra* data suggest that the emission is pointlike, restricting the size of the source $\lesssim 2000$ AU at 2.3 kpc. This emission might be produced by collisionally heated shocks from the fast winds from η Car or perhaps the fast moving outflow from the WWC with the ambient gas, or it might be associated with shocked gas that is intrinsic to the wind of η Car.

11. X-ray emission within $3'$ from η Car can be reproduced by two emission components with interstellar absorption: cool plasma with $kT \sim 0.25$ keV (perhaps coming from the diffuse emission and HDE 303308), and hot plasma with $kT \sim 2.6$ keV or power law $\Gamma \sim 2.5$, perhaps coming from a cluster of young stars. Correcting for these emission components is important in understanding the X-ray spectrum of η Car derived from lower spatial resolution X-ray observatories like *ASCA* and *Suzaku*.

12. Emission from the outer ejecta did not vary significantly on timescales of several years. The slope of the highest energy emission associated with the spectrum of the outer ejecta can be reproduced with $kT \sim 0.6$ keV, which is consistent with the highest temperature derived from analysis of the emission-line spectrum (Leutenegger et al. 2003).

Currently, there are few reasons to suspect that the variable X-ray emission is not driven by shocks produced by the WWC from binary stars. For the first time, the spatially resolved observations of η Car obtained by *XMM-Newton* and *Chandra* have revealed the details of the plasma and absorption components that are directly associated with the WWC plasma. While the earlier spectral analysis of Pittard & Corcoran (2002) did not account for the different emission components identified in this work, their fit was largely determined by emission above 2 keV, which we have shown is dominated by emission from the WWC at the phase of their analysis.

Still the biggest mystery is the cause of the X-ray minimum, which is difficult to fully explain by occultation by a smooth wind from the primary star. If the X-ray activity really switches off during the minimum, a fading of the X-ray emission can be imaged in principle using the scattered X-ray emission from the Homunculus Nebula. The intensity of the Fe K-shell fluorescence line just after the onset of the 2003 minimum should change differently between the eclipsing model and the fading model, and perhaps detailed monitoring of this line by spatially resolved X-ray spectral observations could decide the issue. On the other hand, deformation of the Fe xxv line profiles is unusual in the context of stellar systems, although similar deformation has been noted in iron lines arising from regions of strong gravity near black holes. This feature requires further study with high-resolution spectrometers such as an X-ray microcalorimeter to produce sufficient spectral resolution at 7 keV.

Facilities: XMM(EPIC), CXO(ACIS-S, HETG), ASCA(GIS), ROSAT(PSPC-B)

REFERENCES

Akashi, M., Soker, N., & Behar, E. 2006, ApJ, 644, 451
Anders, E., & Grevesse, N. 1989, Geochim. Cosmochim. Acta, 53, 197
Aschenbach, B., Briel, U. G., Haberl, F., Bräuninger, H. W., Burkert, W., Oppitz, A., Gondoin, P., & Lumb, D. H. 2000, Proc. SPIE, 4012, 731
Balucinska-Church, M., & McCammon, D. 1992, ApJ, 400, 699
Berghöfer, T. W., Schmitt, J. H. M. M., Danner, R., & Cassinelli, J. P. 1997, A&A, 322, 167
Cassinelli, J. P., Miller, N. A., Waldron, W. L., MacFarlane, J. J., & Cohen, D. H. 2001, ApJ, 554, L55
Corcoran, M. F. 2005, AJ, 129, 2018
Corcoran, M. F., Fredericks, A. C., Petre, R., Swank, J. H., & Drake, S. A. 2000, ApJ, 545, 420
Corcoran, M. F., Ishibashi, K., Davidson, K., Swank, J. H., Petre, R., & Schmitt, J. H. M. M. 1997, Nature, 390, 587

Corcoran, M. F., Ishibashi, K., Swank, J. H., & Petre, R. 2001a, ApJ, 547, 1034
Corcoran, M. F., Rawley, G. L., Swank, J. H., & Petre, R. 1995, ApJ, 445, L121
Corcoran, M. F., et al. 1993, ApJ, 412, 792
———. 1998, ApJ, 494, 381
———. 2001b, ApJ, 562, 1031
———. 2004, ApJ, 613, 381
Cox, P., Mezger, P. G., Sievers, A., Najarro, F., Bronfman, L., Kreysa, E., & Haslam, G. 1995, A&A, 297, 168
Damineli, A. 1996, ApJ, 460, L49
Davidson, K. 1999, in ASP Conf. Ser. 179, Eta Carinae at The Millennium, ed. J. A. Morse, R. M. Humphreys, & A. Damineli (San Francisco: ASP), 304
———. 2002, in ASP Conf. Ser. 262, The High Energy Universe at Sharp Focus: *Chandra* Science, ed. E. M. Schlegel & S. D. Vrtilek (San Francisco: ASP), 267
Davidson, K., Dufour, R. J., Walborn, N. R., & Gull, T. R. 1984, in IAU Symp. 105, Observational Tests of the Stellar Evolution Theory, ed. A. Maeder & A. Renzini (Dordrecht: Kluwer), 261
Davidson, K., Ebbets, D., Weigelt, G., Humphreys, R. M., Hajian, A. R., Walborn, N. R., & Rosa, M. 1995, AJ, 109, 1784
Davidson, K., & Humphreys, R. M. 1997, ARA&A, 35, 1
Davidson, K., Walborn, N. R., & Gull, T. R. 1982, ApJ, 254, L47
Davidson, K., et al. 2005, AJ, 129, 900
den Herder, J. W., et al. 2001, A&A, 365, L7
Duncan, R. A., White, S. M., Lim, J., Nelson, G. J., Drake, S. A., & Kundu, M. R. 1995, ApJ, 441, L73
Evans, N. R., Seward, F. D., Krauss, M. I., Isobe, T., Nichols, J., Schlegel, E. M., & Wolk, S. J. 2003, ApJ, 589, 509
Feast, M., Whitelock, P., & Marang, F. 2001, MNRAS, 322, 741
Gayley, K. G., Owocki, S. P., & Cranmer, S. R. 1997, ApJ, 475, 786
Hamaguchi, K., et al. 2007, PASJ, 59, 151
Hillier, D. J., Davidson, K., Ishibashi, K., & Gull, T. 2001, ApJ, 553, 837
Inoue, H. 1985, Space Sci. Rev., 40, 317
Ishibashi, K., Corcoran, M. F., Davidson, K., Swank, J. H., Petre, R., Drake, S. A., Damineli, A., & White, S. 1999, ApJ, 524, 983
Ishibashi, K., et al. 2003, AJ, 125, 3222
Jansen, F., et al. 2001, A&A, 365, L1
Kahn, S. M., et al. 2001, A&A, 365, L312
Kamata, Y., Koyama, K., Tsuboi, Y., & Yamauchi, S. 1997, PASJ, 49, 461
Kitamoto, S., & Mukai, K. 1996, PASJ, 48, 813
Kitamoto, S., Tanaka, S., Suzuki, T., Torii, K., Corcoran, M. F., & Waldron, W. 2000, Adv. Space Res., 25, 527
Leutenegger, M. A., Kahn, S. M., & Ramsay, G. 2003, ApJ, 585, 1015
Lotz, W. 1967, ApJS, 14, 207
Martin, J. C., Davidson, K., Humphreys, R. M., Hillier, D. J., & Ishibashi, K. 2006, ApJ, 640, 474

Martin, J. C., & Koppelman, M. D. 2004, AJ, 127, 2352
Mewe, R., Kaastra, J. S., & Liedahl, D. A. 1995, Legacy, 6, 16
Miller, N. A., Cassinelli, J. P., Waldron, W. L., MacFarlane, J. J., & Cohen, D. H. 2002, ApJ, 577, 951
Morrison, R., & McCammon, D. 1983, ApJ, 270, 119
Pittard, J. M., & Corcoran, M. F. 2002, A&A, 383, 636
Pittard, J. M., & Stevens, I. R. 1997, MNRAS, 292, 298
Pittard, J. M., Stevens, I. R., Corcoran, M. F., & Ishibashi, K. 1998, MNRAS, 299, L5
Pollock, A. M. T., Corcoran, M. F., Stevens, I. R., & Williams, P. M. 2005, ApJ, 629, 482
Scarsi, L. 1993, A&AS, 97, 371
Seward, F. D., Butt, Y. M., Karovska, M., Prestwich, A., Schlegel, E. M., & Corcoran, M. 2001, ApJ, 553, 832
Smith, N., Davidson, K., Gull, T. R., Ishibashi, K., & Hillier, D. J. 2003a, ApJ, 586, 432
Smith, N., Gehrz, R. D., Hinz, P. M., Hoffmann, W. F., Hora, J. L., Mamajek, E. E., & Meyer, M. R. 2003b, AJ, 125, 1458
Soker, N. 2005, ApJ, 635, 540
Stahl, O., Weis, K., Bomans, D. J., Davidson, K., Gull, T. R., & Humphreys, R. M. 2005, A&A, 435, 303
Steiner, J. E., & Damineli, A. 2004, ApJ, 612, L133
Strüder, L., et al. 2001, A&A, 365, L18
Tagliaferri, G., Covino, S., Fleming, T. A., Gagné, M., Pallavicini, R., Haardt, F., & Uchida, Y. 1997, A&A, 321, 850
Tanaka, Y., Inoue, H., & Holt, S. S. 1994, PASJ, 46, L37
Tanaka, Y., et al. 1995, Nature, 375, 659
Trümper, J. 1984, Adv. Space Res., 3, 483
Tsuboi, Y., Koyama, K., Murakami, H., Hayashi, M., Skinner, S., & Ueno, S. 1998, ApJ, 503, 894
Tsuboi, Y., Koyama, K., Sakano, M., & Petre, R. 1997, PASJ, 49, 85
Turner, M. J. L., et al. 2001, A&A, 365, L27
van Boekel, R., et al. 2003, A&A, 410, L37
van Genderen, A. M., Sterken, C., de Groot, M., & Burki, G. 1999, A&A, 343, 847
Verner, E., Bruhweiler, F., & Gull, T. 2005, ApJ, 624, 973
Viotti, R. F., Antonelli, L. A., Rossi, C., & Rebecchi, S. 2004, A&A, 420, 527
Viotti, R. F., et al. 2002, A&A, 385, 874
Weis, K., Corcoran, M. F., Bomans, D. J., & Davidson, K. 2004, A&A, 415, 595
Weisskopf, M. C., Brinkman, B., Canizares, C., Garmire, G., Murray, S., & Van Speybroeck, L. P. 2002, PASP, 114, 1
Whitelock, P. A., Feast, M. W., Koen, C., Roberts, G., & Carter, B. S. 1994, MNRAS, 270, 364
Yamauchi, S., Koyama, K., Sakano, M., & Okada, K. 1996, PASJ, 48, 719